Advanced NanoBiomed Research

ADVANCED NANOBIOMED RESEARCH Open Access

www.advnanobiomedres.com

RESEARCH ARTICLE OPEN ACCESS

Protein-Template Gold Nanoclusters Induce Differentiation and Modify the Functional Properties of Primary Astrocytes

Roberta Fabbri[1] | Karima Jeneh Perry[2] | Emanuela Saracino[1] | Chiara Lazzarini[1,3] | Anna Mariano[4] | Diletta Spennato[1,3] | Maria Grazia Mola[5] | Maria Grazia Raucci[4] | Alessandro Kovtun[1] | Marianna Barbalinardo[6] | Giorgia Conte[1] | Denis Gentili[6] | Marco Caprini[7,8] | Vincenzo Palermo[1] | Roberto Zamboni[1] | Luigi Ambrosio[4] | Wolfgang Losert[9] | Andrea Candini[1] | Grazia Paola Nicchia[3] | Raj K. Gupta[10] | Valentina Benfenati[1] | Shashi P. Karna[2]

[1]Institute for Organic Synthesis and Photoreactivity (ISOF), National Research Council of Italy (CNR), Bologna, Italy | [2]DEVCOM Army Research Laboratory, ATTN: FCDD-RLA-A, Aberdeen Proving Ground, College Park, Maryland, USA | [3]Department of Biosciences, Biotechnologies and Environment, University of Bari Aldo Moro, Bari, Italy | [4]Institute for Polymers Composites and Biomaterials (IPCB), National Research Council of Italy (CNR), Mostra d' Oltremare, Napoli, Italy | [5]Department of Medicine and Surgery, Libera Università Mediterranea "Giuseppe Degennaro", Casamassima, Italy | [6]Institute for the Study of Nanostructured Materials (ISMN), National Research Council of Italy (CNR), Bologna, Italy | [7]Department of Pharmacy and Biotechnology, (FaBit) University of Bologna, Bologna, Italy | [8]IRCCS, Istituto delle Scienze Neurologiche di Bologna, Bologna, Italy | [9]Department of Physics, University of Maryland, College Park, Maryland, USA | [10]DoD Blast Injury Research Coordination Office, Medical Research and Development Command, Fort Detrick, Maryland, USA

Correspondence: Andrea Candini (andrea.candini@isof.cnr.it) | Valentina Benfenati (valentina.benfenati@isof.cnr.it) | Shashi P. Karna (shashi.p.karna.civ@army.mil)

Received: 24 July 2025 | **Revised:** 2 January 2026 | **Accepted:** 7 January 2026

Keywords: astrocytes | biophotonic | calcium signaling | ion channels | nanoclusters | nanomaterials | Transient Receptor Potential Vanilloid Channel 4

ABSTRACT

Astrocyte ion channels, water channels, and calcium signaling play vital roles in maintaining brain homeostasis, coordinating neural network activity, supporting cognitive functions, and mediating neurovascular coupling. Disruptions in astrocyte dynamics are causally linked to gliosis occurring in pathologies, such as brain injuries and neurological diseases. Despite their importance, the potential to probe and modulate astrocyte molecular, functional, and morphological properties using intracellular light adsorbing nanoscale interfaces has been limited. In this study, we investigate the effects of fluorescent gold nanoclusters (fAuNCs) bound to bovine serum albumin (BSA) on the morphological, molecular, and functional properties of primary rat cortical astrocytes over an extended period. Treatment with fAuNCs-BSA is not toxic over long term and induces notable morphological changes alongside alterations in whole-cell chloride currents, cell volume regulation, and calcium signaling magnitude. To leverage the light-absorbing properties of fAuNCs-BSA, we expose acutely fAuNCs-BSA-treated astrocytes to LED blue light ($\lambda\_ex = 450$ nm), which modulates potassium currents. Nanodiamond thermometry suggests that this effect results from local heating caused by photoexcitation of the nanoclusters. The potential of nanoclusters as a transformative approach for studying astrocyte function and their role in the biophysical mechanisms underlying neural communication is discussed.

Roberta Fabbri, Karima Jeneh Perry and Emanuela Saracino contributed equally to this work.

1 | Introduction

Modern neuroscience revolutionizes the concept of neurons as uniquely responsible for brain cognitive functions [1]. Specifically, in vitro and in vivo studies collected in the past four decades highlighted that the function of glial cells, called astrocytes, is critical for the correct brain homeostasis and physiology [1–3]. Astrocytes play a key role in controlling brain hydrosaline and chemical concentrations in the extracellular space [1, 3]. This is realized mainly by ions and water flow through trans-membrane proteins forming ion channels, water channels, and transporters, and by calcium signaling that can occur within a single astrocyte or propagate through waves via junction coupling [1, 3, 4]. In addition, prior in vivo studies highlighted that the ions and water dynamics of astrocytes are critical for synaptic modulation, memory formation, learning [3], neurovascular coupling [5], metabolism, and regulation of sleep [6]. Dysfunction of these flows in astrocytes plays a causal role during acute and chronic neurological conditions such as glioma, epilepsy, ischemia, and Alzheimer's disease [6–9]. Astrocytes are the major cell types involved in inflammatory gliotic reactions observed in response to the interaction with drug delivery systems and/or bio-electronic and photonic devices [10, 11]. Despite such important roles, astrocytes remain underexplored compared to neurons, partly due to the limited availability of nanotechnologies, appropriate for probing and monitoring their specific functional properties [10, 12, 13].

The use of nanomaterials in biomedicine targeting the study, the monitoring and possibly the therapy of the brain, is rapidly advancing. Their effectiveness largely depends on how they interact with cell membrane and intracellular components [11–15]. Morphological and chemophysical properties of nanomaterials can influence such interactions, impacting cell function and structure across different spatiotemporal scales, from cellular signaling to morphology. Notably, monitoring the effects of nanomaterials on astrocytes is crucial to prevent detrimental processes, such as oxidative stress, cell death, and gliotic inflammation.

Among nanotools, bio-templated fluorescent metal nanoclusters (NCs), in particular the one composed of gold (fAuNCs), have attracted significant attention due to their size-tunable and highly stable fluorescence [16–20]. Synthesized using biological macromolecules as templating agents, bio-templated metal nanoclusters have been extensively used for biomedical imaging of cancerous and healthy cells, biosensing and drug delivery [20, 21].

The broad range of applications of bio-templated metal nanoclusters arises from their quantized electronic states, that strongly interact with their surroundings [14–18], resulting in intense and tunable photoemission ranging from visible to near-infrared (NIR) wavelengths. Additionally, they exhibit higher chemical stability than metal NCs alone [19–21], along with improved biocompatibility with different cell types and organs [22].

Focusing on the nervous system, research on the interaction of fAuNCs with neurons and glia is mainly limited to the study of cytotoxicity, cell imaging and detection of neurotransmitters, showing their suitability for diagnostic, drug delivery and bioimaging purposes [23–30].

Previous studies also described the interaction of nonbio-templated AuNCs with human astrocyte cell lines, showing a size dependent effect [31] and the advantage of AuNCs over commonly used gold nanoparticles (AuNPs) [32]. In this regard, size and surface ligands of AuNCs have been found to influence alteration in astrocytic responses at both organellar and transcription factor levels [31]. On the other side, exposure of organotypic and primary neural cultures to conventional AuNPs has been reported to induce neurotoxicity, dendritic spine density, and glial activation depending on their sizes, shape, and surface coating [32].

Given its multiple versatile binding sites and ability to stabilize gold particles across a wide size range, Bovine Serum Albumin (BSA) plasma protein represents an ideal candidate to be employed as a biological template to guide the formation of Au nanoclusters. To fill the gap present in the literature, we investigated the effect of BSA-templated fAuNCs (fAuNCs-BSA) [18] on the cell viability and morphology of primary astrocytes, and in addition on their physiological properties. In this context, the interactions of bio-templated fAuNCs with astrocytes remain largely unexplored. In particular, it remains unclear how bio-templated fAuNCs surface might interact with ion and water channels and whether such interactions might affect the bioelectrical and functional properties of astrocytes. Moreover, the attractive optical properties of fAuNCs have never been exploited to probe or modulate the physiology of astrocytes.

For these reasons, here we investigated the effects of fAuNCs-BSA on the morphology and physiology of primary astrocytes, both over long term without light exposure and acutely using photostimulation.

We found that astrocytes were healthy after continuous exposure (24 h) to high concentration (1 mM) of fAuNCs-BSA and remained viable up to 3 weeks after the treatment (21 DIV). Incubation of astrocytes with fAuNCs-BSA induced internalization of the nanostructure and a drastic morphological change—"stellation"—of cells that involves large elongations departing from the cell body, which were persistent and growing over several weeks. Patch-clamp, water transport assay and calcium imaging results indicate that the morphological change, which appears to be consistent with cell differentiation, is accompanied by an increase of inward and outward whole-cell membrane chloride currents, of cell regulatory volume capabilities and of calcium oscillations in most of the treated cells. Photostimulation with blue LED light (excitation wavelength, $\lambda_{ex} = 450$ nm) inhibited the K^+ conductance of fAuNCs-BSA treated cells. Nanodiamond (ND) thermometry studies show a heating effect of the fAuNCs upon photostimulation, which possibly contributes to the observed effect on calcium signaling and potassium (K^+) currents. Collectively, our results show that fAuNCs-BSA are a powerful nanoscale tool to differentiate astrocytes and to tune their bioelectrical and functional properties. Future research in this field could provide key insight into biophysical mechanisms governing cell–nanomaterial interaction and its effect on astrocyte differentiation, and on ionic currents, water transport and intracellular signaling pathways involved in this process [33, 34]. Such knowledge could drive the generation of advanced nanomedicine theragnostic applications, holding a significant clinical potential in the glial-targeted diagnosis, and treatment of many severe neurological disorders.

2 | Results and Discussion

2.1 | fAuNCs-BSA Promote Astrocyte Star-Like Morphology

The chemo-physical properties of bio-templated fluorescent metal nanoclusters have been extensively studied [19–22]. However, given that morphology, shape, and surface z-potential are critical for the uptake and distribution of fAuNCs inside cells [22], at first, we sought to perform scanning electron microscopy (SEM), transmission electron microscopy (TEM), dynamic Light Scattering (DLS), and surface z-potential (SZP) analysis on [1 mM] fAuNCs-BSA. Figure S1 shows fAuNCs-BSA particles casted on a glass coverslip from cell media and left to dry. Round-shaped clusters ranging from a few nanometers to around 100–200 nm were observed. Small, rounded particles were visible (Figure S1B), along with larger aggregates exhibiting regular geometric shapes (see inset of Figure S1A), which likely originated from crystallization occurring during the drying process. These observations align with the DLS analysis, that reveals an average particle size of 150 ± 20 nm. The surface z-potential was found to be −30 ± 2 mV. Considering the possible influence of fAuNCs-BSA size and surface charge on cytotoxicity [22], we analyzed the impact of fAuNCs-BSA on astrocyte viability. Primary rat cortical astrocytes, seeded on poly-D-lysine (PDL)-coated glass coverslips, were incubated for 24 h with different concentrations of fAuNCs-BSA ([0.1 mM], [1 mM]). fAuNCs-BSA, were synthetized as previously reported [16] and described in the Materials and Methods section. Further details on the morphological characterization are reported in the Supporting Information section (Figure S1). 24 h after the treatment, cells were labeled with fluorescein diacetate (FDA) and Hoechst 33342 to mark the cell nuclei (Figure S2). Green, fluorescent viable cells were visible in all analyzed samples (Figure S2A–C). Notably, cells treated with [1 mM] fAuNCs-BSA were viable and displayed a star-like morphology, typical of differentiated astrocytes in vitro [33–36]. On the other hand, cells treated with [0.1 mM] fAuNCs-BSA maintain the same polygonal morphology described for pure primary culture of rodent astrocytes [37–39], observed in not treated (NT) cells (Figure S2 B). Viable/dead cell assay indicates that 99% of the cells were viable, after the treatment with [0.1 mM] and [1 mM] fAuNCs-BSA (Figure S2 D). Given the preliminary observation of the effect of [1 mM] fAuNCs-BSA on astrocyte morphology, we sought to analyze its effect on cell viability, metabolism, and morphological properties over longer time intervals. In the following, we focus on this specific concentration, chosen as the lowest one at which the differentiation effect is observed.

The interaction of unbounded AuNCs with human astrocytes cell line has been previously described, showing a size dependent effect [31] and highlighting the advantages of using AuNCs over conventional gold nanoparticles (AuNPs) [32]. However, previous studies did not address any possible effects on astrocytes' morphology. FDA/Hoechst confocal imaging, viable/dead cell assay, cell counting, and differentiation analyses were performed 24 h, 3 days in vitro (3DIV), 14 DIV, and 21 DIV after the treatment with fAuNCs-BSA [1 mM] (Figure 1). Low magnifications (20X) confocal images of FDA/Hoechst-stained NT and fAuNCs-BSA [1mM] astrocytes, captured at 24 h, 3 DIV, 14 DIV, and 21 DIV are reported in Figure 1A.

We confirmed that viable NT cells maintained a polygonal flat shape over time, resembling the one of in vitro primary astrocytes grown on smooth glass-coated surfaces or biomaterials such as polystyrene Petri dishes and silk fibroin biopolymers [33, 34, 37–39] (Figure 1A, upper panels). On the other hand, [1 mM] fAuNCs-BSA-treated astrocytes were viable and displayed a differentiated phenotype, which persists over time, with elongations originating from the cell body and extending their end-feet on distal cells (Figure 1A, lower panels).

The analyses of the % of living cells indicated that almost 100% of astrocytes remained viable in NT as well as in [1mM] fAuNCs-BSA treated conditions, even after 21 DIV (Figure 1B). No significant difference was observed in the nominal number of living cells between NT and [1 mM] fAuNCs-BSA treated astrocytes at all the time points considered in the analyses (Figure 1C). Interestingly, the number of viable cells per area in both conditions was variable over time, increasing up to 14 DIV and then decreasing after 21 DIV (Figure 1C).

Alamar Blue assay (AB), an assay that measures the cell metabolism [33, 39], indicates that cell metabolic activity progressively increases from 3 to 14 and 21 DIV in both NT and [1 mM] fAuNCs-BSA-treated astrocytes, thereby confirming the absence of cytotoxic effects at [1 mM]. However, at 21 DIV, [1 mM] fAuNCs-BSA-treated astrocyte metabolic activity was significantly lower than NT cells (Figure 1D). The lower metabolic activity observed in [1 mM] fAuNCs at 21 DIV compared with 14 DIV is consistent with the significantly lower number of cells/area observed between the same time points (14 DIV vs. 21 DIV) in [1 mM] fAuNCs.

Chloroauric acid salt (HAuCl4) is the precursor to synthetize unbounded fAuNCs [40]. Thus, we sought to incubate astrocytes with HAuCl4 at the same concentration of fAuNCs-BSA (1 mM), as internal control to assess the safety of unbounded fAuNCs, and repeat a comparative analysis of cell metabolism. The AB assay reported in Figure S3 indicates that, for each time point tested, cell viability was higher in cells treated with fAuNCs-BSA, with respect to the cells treated with [1mM] HAuCl4. The result confirmed that BSA binding to fAuNCs ameliorates the biocompatibility of metal NCs (Figure S3) [16, 41].

A previous study in human astrocytes cell line indicated that unbounded AuNCs size play a critical role in regulating organelle and redox-responsive transcription factor expression [31].

To verify if the change in astrocytes shape could be due to an oxidative stress response to the material internalization, reactive oxigen species (ROS) production was assessed using DCFH-DA assay. NT astrocytes and astrocytes treated with [1 mM] BSA were considered as negative control, whereas cells treated with Fenton's reagent (H_2O_2/Fe^{2+} 2 mM) were considered as positive control for ROS production. At 3DIV, the fluorescence intensity of DCFH-DA in [1 mM] fAuNCs-BSA-treated, [1 mM] BSA-treated, and NT samples was comparable, and significantly lower than the one observed by treating cells with Fenton reagent. In line with previous studies performed in different cell lines [31] our data clearly indicated that at 3 DIV, [1 mM] fAuNCs-BSA do not induce ROS production (Figure S4), confirming that morphological differentiation observed already at 3DIV is not due to a stress response.

Given the comparable viability between NT and [1 mM] fAuNCs-BSA-treated astrocytes, and the absence of induced ROS production in fAuNCs-BSA-treated, we hypothesized that the lower

metabolic activity observed over the long term could be due to the dominance of the differentiation process occurring in astrocytes treated with fAuNCs-BSA [42, 43]. To get further insight, low and high magnification morphological observations (Figure 1E) and quantitative cell morphometric analyses (Figure 1F,G) were performed at the same time points (24 h, 3 DIV, 14 DIV, 21 DIV) on NT and [1 mM] fAuNCs-BSA-treated astrocytes.

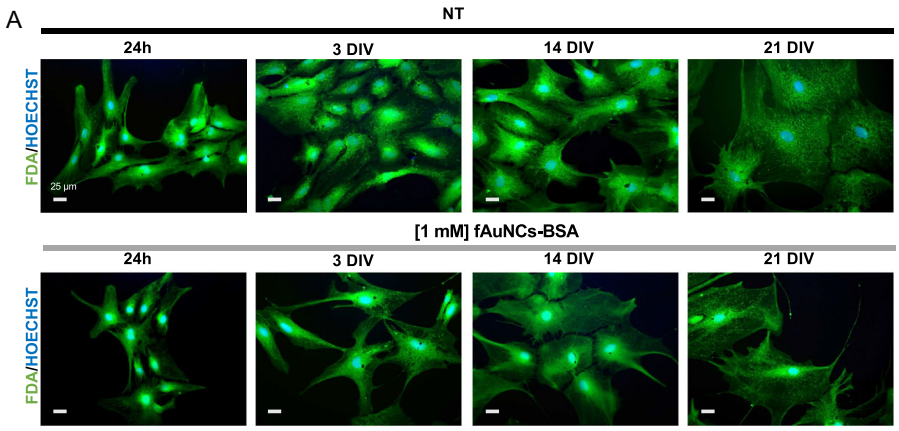

FIGURE 1 | Impact of fAuNCs-BSA on viability and morphology of astrocytes. (A) Low magnification (20X) confocal images of FDA/Hoechst stained astrocytes: Not treated cells (NT, upper panels) and fAuNCs-BSA [1 mM] (lower panels) treated cells, captured at 24 h, 3 DIV, 14 DIV, and 21 DIV. Scale bar is 25 µm. (B) Bar dot plot reporting the averaged ratio between viable cells and the total number of cells per image (FDA^+-$Hoechst^+$/ Total number of Hoechst+ cells) calculated on NT and fAuNCs-BSA [1 mM] treated samples after 24 h, 3 DIV, 14 DIV, and 21 DIV. (C) Bar plot reporting the average number of living cells/area calculated on NT and fAuNCs-BSA [1 mM] treated samples at 24 h, 3DIV, 14DIV, and 21 DIV. For 24 h, $n = 65$ for NT and $n = 64$ for fAuNCs-BSA [1 mM]; for 3 DIV, $n = 75$ for NT and $n = 78$ for fAuNCs-BSA [1 mM]; for 14 DIV, $n = 78$ for NT and $n = 75$ for fAuNCs-BSA [1 mM]; for 21 DIV, $n = 76$ for NT and $n = 76$ for fAuNCs-BSA [1 mM] (n = number of images analyzed from 3 independent experiments). (D) Alamar Blue cell metabolism assay performed on the NT and fAuNCs-BSA [1 mM] treated astrocytes at 3DIV, 14DIV, and 21 DIV. $n = 3$ for 3 DIV, $n = 5$ for 14 DIV, $n = 13$ for 21 DIV (n = number of measurements, respectively, for NT and fAuNCs-BSA [1 mM] conditions). (E) High magnification (40X) confocal images of FDA/Hoechst stained astrocytes: Not treated cells (NT, upper panels) and fAuNCs-BSA [1 mM] (lower panels) treated cells, captured at 24 h, 3DIV, 14DIV, and 21 DIV. Scale bar is 25 µm. (F) Bar-dot plot reporting the averaged ratio between differentiated astrocytes and the total number of viable cells calculated on NT and fAuNCs-BSA [1 mM] treated astrocytes after 24 h, 3DIV, 14DIV and 21 DIV. For 24 h, $n = 65$ for NT and $n = 64$ for fAuNCs-BSA [1 mM]; for 3 DIV, $n = 75$ for NT and $n = 78$ for fAuNCs-BSA [1 mM]; for 14 DIV, $n = 78$ for NT and $n = 75$ for fAuNCs-BSA [1 mM]; for 21 DIV, $n = 76$ for NT and $n = 76$ for fAuNCs-BSA [1 mM] (n = number of images analyzed from 3 independent experiments). (G) Number of elongation (processes) departing from astrocytes cell body after 24 h, 3DIV, 14DIV, and 21 DIV. For 24 h, $n = 33$ for NT and $n = 32$ for fAuNCs-BSA [1 mM]; for 3 DIV, $n = 32$ for NT and $n = 38$ for fAuNCs-BSA [1 mM]; for 14 DIV, $n = 39$ for NT and $n = 37$ for fAuNCs-BSA [1 mM]; for 21 DIV, $n = 38$ for NT and $n = 38$ for fAuNCs-BSA [1 mM] (n = number of images analyzed from 3 independent experiments). Data are reported as mean ± SE. Statistical significance was calculated via one-way ANOVA with Bonferroni post-test. *: $p < 0.05$, **: $p < 0.01$, ***: $p < 0.001$. No statistical difference was observed in the ratio viable/total cells (%) between NT and fAuNCs-BSA [1 mM] at 24 h ($p = 0.6$), 3 DIV ($p = 0.26$), 14 DIV ($p = 0.6$), and 21 DIV ($p = 0.48$). Statistical difference was observed in the n° viable cells/area between NT and fAuNCs-BSA [1 mM] at 24 h ($p = 0.04$). No statistical difference was observed in the n° viable cells/area between NT and fAuNCs-BSA [1 mM] at 3DIV ($p = 0.26$), at 14 DIV ($p = 0.7$), at 21 DIV ($p = 0.89$). No statistical difference was observed in the n° viable cells/area for NT between 24 h and 3 DIV ($p = 0.18$), 24 h and 14 DIV ($p = 0.19$), 24 h and 21 DIV ($p = 0.08$). Statistical difference was observed in the n° viable cells/area for fAuNCs-BSA [1 mM] between 24 h and 3 DIV ($p = 0.03$), 24 h and 21 DIV ($p = 0.0013$). No statistical difference was observed in the n° viable cells/area for fAuNCs-BSA [1 mM] between 24 h and 14 DIV ($p = 0.2$). Statistical difference was observed in the % of reduced AB between NT and fAuNCs-BSA [1 mM] at 21 DIV ($p = 0.0039$). No statistical difference was observed in the % of reduced AB between NT and fAuNCs-BSA [1 mM] at 3 DIV (0.24) and at 14 DIV (0.84). Statistical difference was observed in ratio differentiated/total cells (%) between NT and fAuNCs-BSA [1 mM] at 3 DIV ($p = 0.0028$), at 14 DIV ($p = 0.021$), at 21 DIV ($p = 0.0032$). No statistical difference was observed in ratio differentiated/total cells (%) between NT and fAuNCs-BSA [1 mM] at 24 h ($p = 0.52$). Statistical difference was observed in ratio differentiated/total cells (%) for fAuNCs-BSA [1 mM] between 24 h and 3 DIV ($p = 0.0009$). No statistical difference was observed in ratio differentiated/total cells (%) for NT between 24 h and 3 DIV ($p = 0.33$), between 24 h and 14 DIV ($p = 0.89$), between 24 h and 21 DIV ($p = 0.64$), between 14 DIV and 21 DIV ($p = 0.73$), between 3 DIV and 14 DIV ($p = 0.25$), between 3 DIV and 21 DIV ($p = 0.15$). No statistical difference was observed in ratio differentiated/total cells (%) for fAuNCs-BSA [1 mM] between 24 h and 14 DIV ($p = 0.16$), between 24 h and 21 DIV ($p = 0.07$), between 14 DIV and 21 DIV ($p = 0.67$), between 3 DIV and 14 DIV ($p = 0.06$), between 3 DIV and 21 DIV ($p = 0.15$). Statistical difference was observed in n° processes between NT and fAuNCs-BSA [1 mM] at 3 DIV ($p < 0.0001$), at 21 DIV ($p = 0.0007$). Statistical difference was observed in n° processes for NT between 24 h and 3 DIV ($p = 0.0083$). Statistical difference was observed in n° processes for fAuNCs-BSA [1 mM] between 24 h and 3 DIV ($p = 0.05$), between 3 DIV and 14 DIV ($p = 0.008$). No statistical difference was observed in n° processes between NT and fAuNCs-BSA [1 mM] at 24 h ($p = 0.25$) and at 14 DIV ($p = 0.43$). No statistical difference was observed in n° processes for NT between 24 h and 14 DIV ($p = 0.9$), between 24 h and 21 DIV ($p = 0.29$), between 14 DIV and 21 DIV ($p = 0.44$), between 3 DIV and 14 DIV ($p = 0.07$), between 3 DIV and 21 DIV ($p = 0.21$). No statistical difference was observed in n° processes for fAuNCs-BSA [1 mM] between 24 h and 14 DIV ($p = 0.64$), between 24 h and 21 DIV ($p = 0.26$), between 14 DIV and 21 DIV ($p = 0.07$), between 3 DIV and 14 DIV ($p = 0.06$), between 3 DIV and 21 DIV ($p = 0.3$).

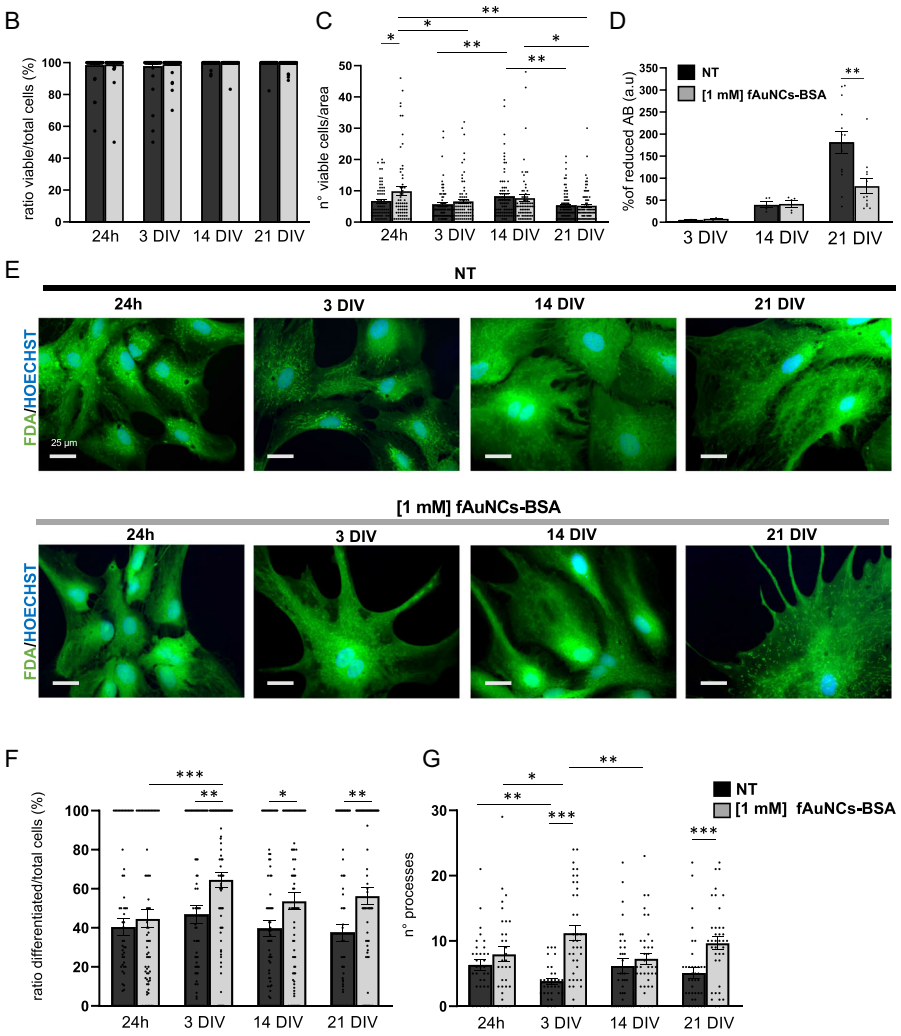

FIGURE 1 | Continued.

It can be observed that, for each time point analyzed, only [1 mM] fAuNCs-BSA-treated astrocytes displayed a strong differentiated phenotype. Cell differentiation morphometric analyses, performed with methods previously described [33], indicated that the % of differentiated astrocytes was significantly higher in cells treated with fAuNCs-BSA [1 mM] compared with NT cells (Figure 1F).

It is worth noting that the % of differentiated cells in fAuNCs-BSA-treated astrocytes is higher than NT at each time point analyzed, from 3 DIV to 21 DIV, and is long-lasting up to 3 weeks after the treatment (Figure 1F). Interestingly, the number of elongations (processes) departing from astrocytic cell body changes over time. These results support the tenet that the differentiation induced by fAuNCs-BSA is a dynamic event, possibly involving structural cytoskeletal changes and dynamic of actin, as previously described for astrocytes [44].

In this context, our study reports the first application of bio-templated AuNCs in primary astrocytes, providing the earliest evidence of cellular differentiation induced by the treatment [45, 46].

Since morphological alteration might occur upon inflammatory gliotic reaction, possibly induced by interaction of astrocytes with nanomaterials [10, 11, 36], we evaluated the distribution and expression level of Glial Fibrillar Acid Protein (GFAP), a typical marker of astrogliosis, by confocal microscopy and GFAP + cell quantification, as well as western immunoblotting of GFAP and densitometric analyses in NT and fAuNCs-BSA-treated astrocytes (Figure 2). In agreement with previous studies using the same protocol to prepare primary rat neocortical astrocytes [33–39], analyses of confocal imaging confirmed the purity of the cell culture and that nearly 100% of [1 mM] fAuNCs-BSA-treated cells were indeed astrocytes (Figure 2A–C). Immunoblotting revealed that the expression levels of GFAP were comparable between NT and fAuNCs-BSA-treated astrocytes, thereby indicating that fAuNCs-BSA do not promote gliotic reactions in vitro (Figure 2D). This result suggests that the morphological alteration observed in astrocytes treated with fAuNCs-BSA is not attributable to a harmful effect of nanomaterial-induced astrogliosis, but it could be possibly correlated with a different biophysical mechanism.

2.2 | fAuNCs-BSA Internalize Into Astrocytes Organelles Without Inducing ROS

To gain insights into the interaction and possible internalization of fAuNCs-BSA into astrocytes, we imaged cells with SEM at different magnifications. We also performed elemental analysis of

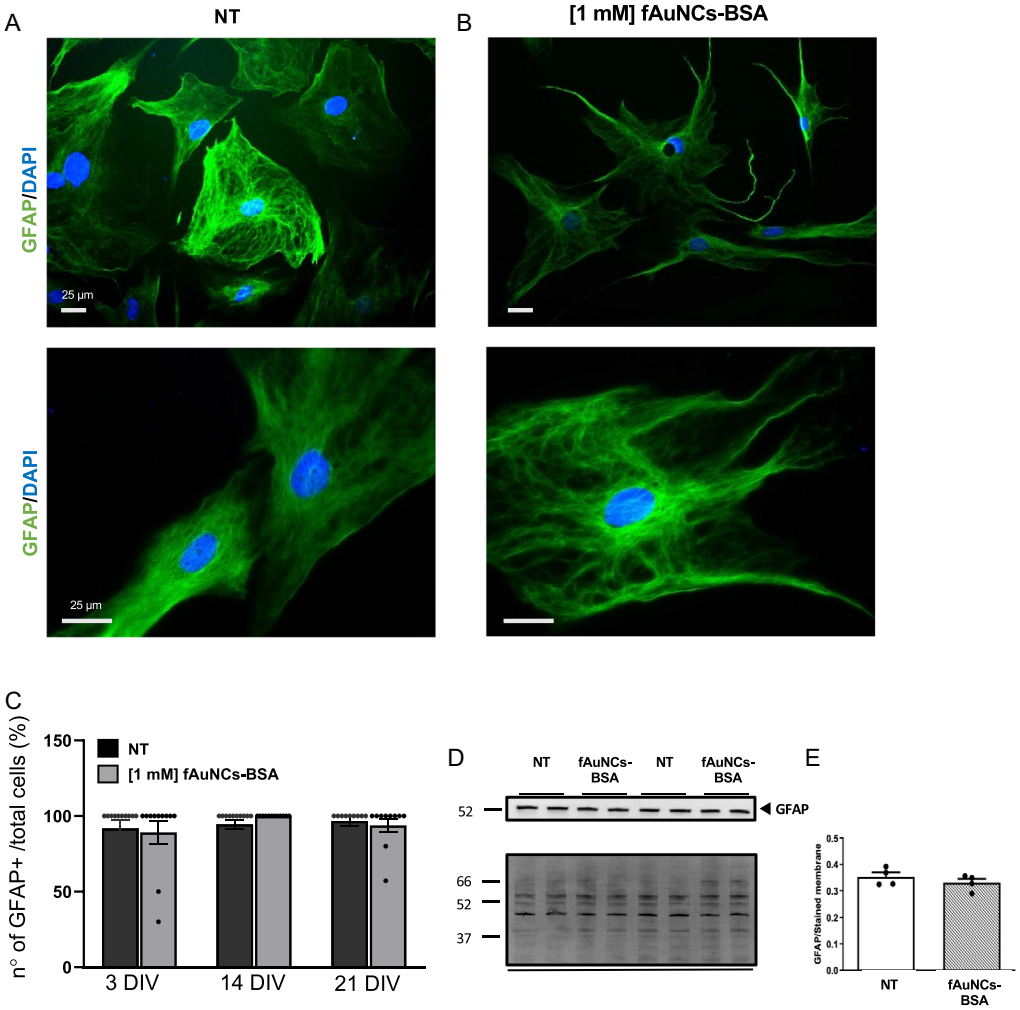

FIGURE 2 | fAuNCs-BSA do not induce gliotic reactions in astrocytes. (A,B) Low magnification (20X, upper panels) and high magnification (40X, lower panels) confocal images of NT and fAuNCs-BSA [1 mM]-treated astrocytes stained with GFAP. Scale bar is 25 µm. (C) Bar dot plot graph reporting the n° of GFAP+ /total cells (%). Note that all the cells were $GFAP^+$ positive ($n = 12$ for 3 DIV, $n = 12$ for 14 DIV, $n = 10$ for 21 DIV, $n =$ number of images analyzed, respectively for NT and fAuNCs-BSA [1 mM] conditions). (D) Western Blot analyses and (E) bar dot plot of quantitative densitometry of GFAP expression ($n = 4$ per condition, $n =$ number of experiments). Data are reported as mean ± SE. Statistical significance was calculated via one-way ANOVA with Bonferroni post-test. *: $p < 0.05$, **: $p < 0.01$, ***: $p < 0.001$. No statistical difference was observed in n° of GFAP+ /total cells (%) between NT and fAuNCs-BSA [1 mM] at 3 DIV ($p = 0.78$), at 14 DIV ($p = 0.10$) and at 21 DIV ($p = 0.6$).

NT and fAuNCs-BSA [1 mM]-treated cells (Figure 3) using X-ray energy dispersive spectroscopy (EDS). SEM image (Figure 3A) confirms the polygonal and undifferentiated morphology of NT cells. In contrast, fAuNCs-BSA-treated cells were highly differentiated with long branches ending distantly in leaflets and lamellipodia protrusions (Figure 3B). Notably, higher magnification images show the presence of bright aggregates with variable sizes, which are also visible inside the cellular body, in particular at the end-feet of the protrusions (Figure 3B, arrows), suggesting the presence of fAuNCs-BSA also within the cells. This is evidenced from the EDS spectrum (Figure 3C), performed on the images captured from NT cells (Figure 3C) and [1 mM] fAuNCs-BSA treated cells (Figure 3D). The spectra taken on NT and fAuNCs-BSA-treated cells (respectively Figure 3C,D) show the presence of both carbon and gold only in the cells treated with fAuNCs-BSA, while only carbon is present in NT cells. This colocalization of carbon (deriving from the cells) and gold (from the nanoclusters) only in fAuNCs-BSA cells strongly supports the observation that the nanoclusters are present within the cells.

To further validate this observation and get deeper insight into nanocluster localization within cell components, we performed confocal imaging of fAuNCs-BSA-treated astrocytes, labeled with Mito-tracker Red staining. Figure 3E suggests the diffusion of fAuNCs-BSA likely in correspondence with mitochondria, as indicated by the red fluorescence emission (from the particles and labeled mitochondria). To enable a more accurate discrimination of intracellular fAuNCs-BSA nanostructures, scanning transmission electron microscope (STEM) was performed on NT and fAuNCs-BSA-treated astrocytes (Figure 3F,G). Figure 3G clearly shows that in treated cells, fAuNCs-BSA localizes mostly within the inner membrane of astrocytic mitochondria (labeled as "m" in Figure 3F,G, as evidenced from the darker regions, indicated by the red arrows). The inset in Figure 3F corresponds to the zoomed-in region of the high-contrast (lighter) area in the larger image. Mitochondria were identified based on their characteristic

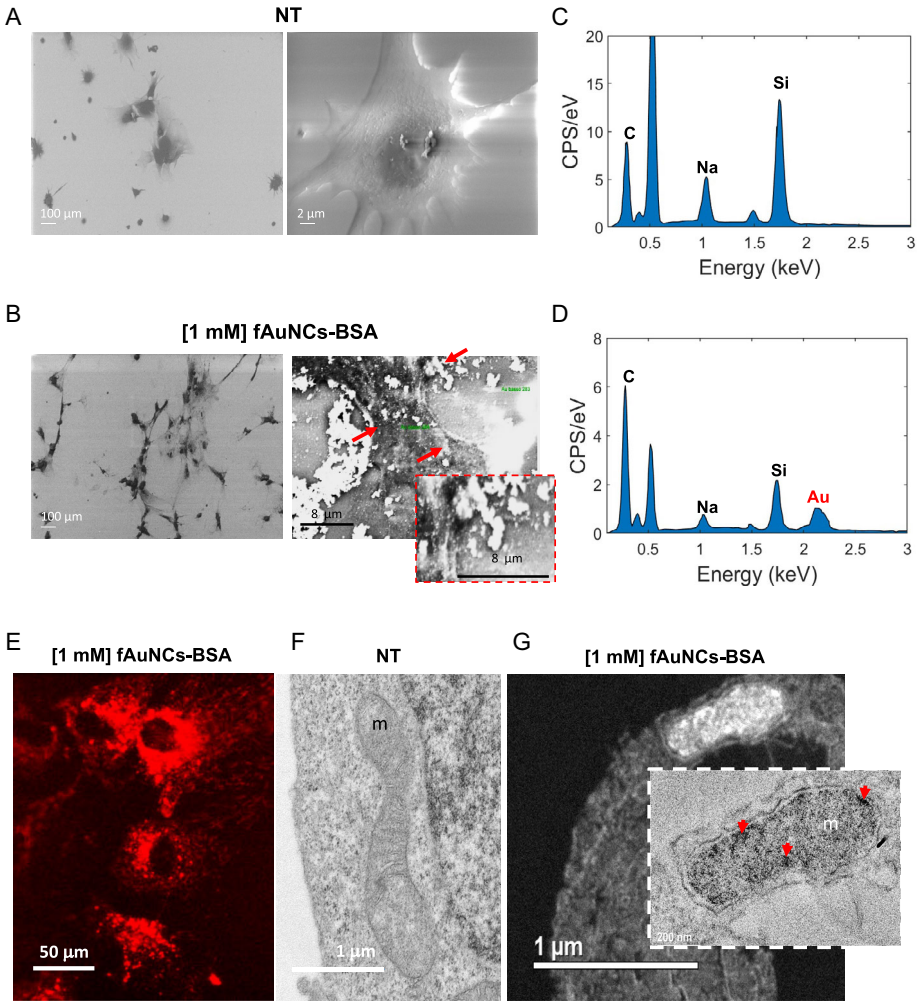

FIGURE 3 | fAuNCs-BSA internalize into astrocyte organelles. (A,B) SEM imaging and microanalysis of (A) NT and (B) fAuNCs-BSA [1 mM] treated astrocytes. Scale bars in (A) are 100 µm (left panel), 2 µm (right panel). Scale bars in (B) are 100 µm (left panel), 8 µm (right panel). Red arrows (Figure (B) indicate the portion where X-ray energy dispersive spectra (EDS) have been performed (inset: higher magnification, scale bar is 8 µm). (C,D) X-ray EDS of elemental analysis confirming the presence of gold (Au) with carbon (C) atoms in fAuNCs-BSA [1 mM]-treated astrocytes (panel D) while Au is not present in NT astrocytes (panel C). (E) Confocal microscopy image of fAuNCs-BSA treated astrocytes stained with Mito-track (red) suggests localization of particles in the mitochondria. Scale bar is 50 µm. (F,G) STEM of NT and fAuNCs-BSA treated astrocytes (inset: higher magnification, scale bar is 200 nm) suggesting that the fAuNCs-BSA (visible as the darker areas, as indicated by the red arrows) are localized mostly inside cell mitochondria (m) organelles. Scale bar is 1 µm.

double-membrane structure and size. These results confirm the specificity of the black dots as the fAuNCs-BSA nanoparticles.

The absorbance and emission properties of fAuNCs-BSA have been widely documented in literature [16]. We sought to leverage these chemophysical properties of fAuNCs-BSA and perform fluorescence imaging on NT astrocytes, treated with [1 mM] BSA alone and with [1 mM] fAuNCs-BSA, stained with Hoechst to mark the cell nuclei. Representative fluorescent images, collected using a blue LED light ($\lambda_{ex} = 470$ nm) equipped fluorescence microscope, revealed that, while NT and BSA-treated cells were dark (Figure 4A,B), astrocytes incubated with fAuNCs-BSA (Figure 4C) emitted a strong red fluorescence.

We also performed a spectrophotometric analysis of fluorescence emission spectra of NT, [1 mM] BSA and [1 mM] fAuNCs-BSA-treated cells and of the solutions used for astrocyte treatment (Figure 4D,E), by exciting at 360 nm and 480 nm and collecting fluorescence spectra within 500–800 nm. It is highlighted that cells treated with fAuNCs-BSA display averaged fluorescence emission spectra peaked at 650 nm either with $\lambda_{ex} = 360$ and $\lambda_{ex} = 480$ nm [18]. Notably, the latter peak is not visible neither in cells treated with BSA nor in NT cells. The fluorescence emission spectra recorded in fAuNCs-BSA-treated cells closely overlap with the ones recorded for the fAuNCs-BSA solution. The averaged fluorescence emission spectra at $\lambda_{ex} = 360$ nm and $\lambda_{ex} = 480$ nm were comparable in the presence and absence of cells, for both BSA and fAuNCs-BSA conditions. On the contrary, the shape of the fluorescence emission spectrum of NT cells at both $\lambda_{ex} = 360$ and $\lambda_{ex} = 480$ nm closely resembled that of cells treated only with BSA. These results show that BSA does not change the spectral properties of the cells whereas the nanoparticles do, consistent with the presence of fAuNCs-BSA on the cells.

Previous studies on the nontumorigenic mouse microglia [28–30, 32], indicate that fAuNCs disperse mainly in cell cytoplasm or in the organelles. [32] Possibly, as supported by previous

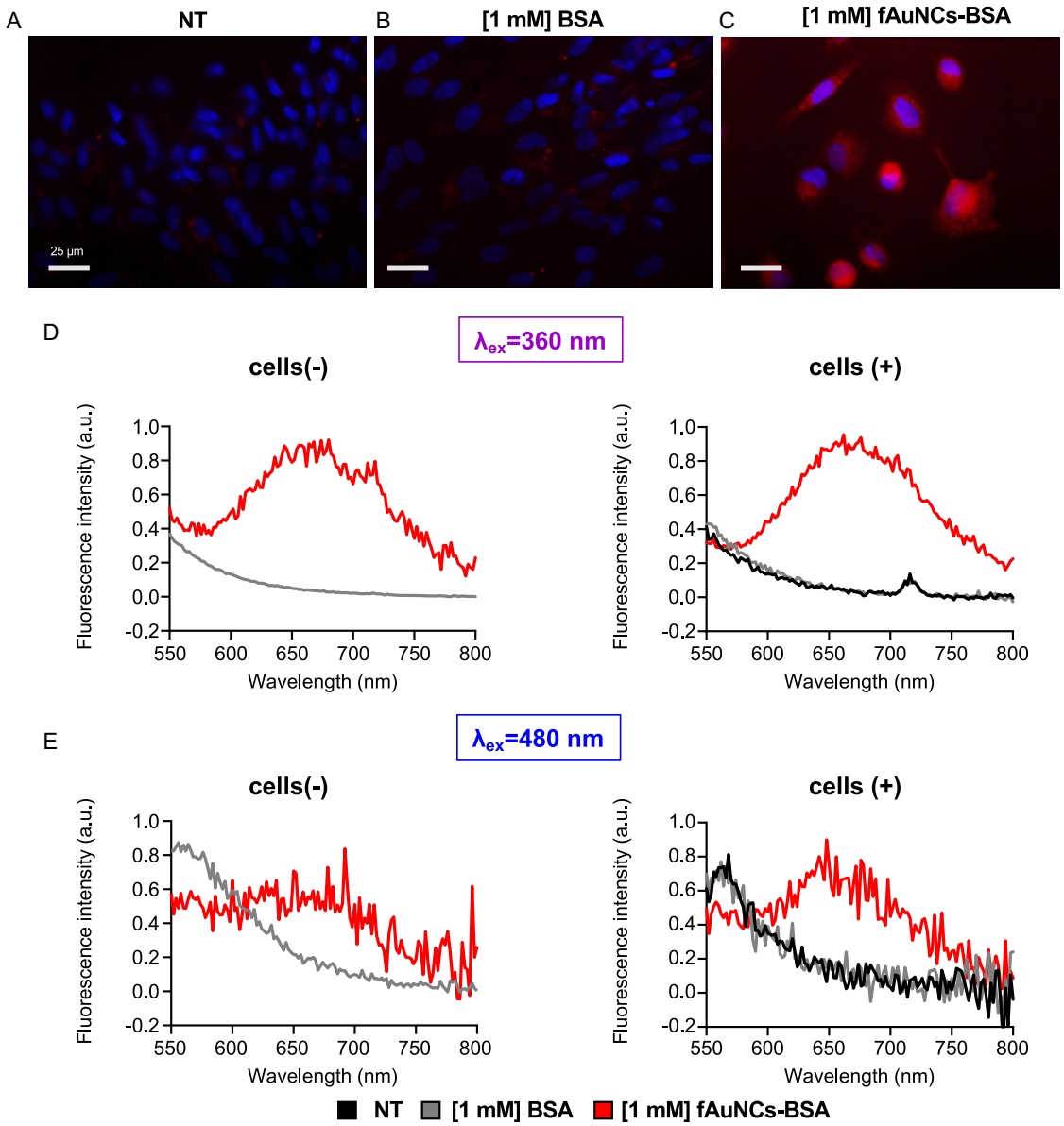

FIGURE 4 | Spectral properties of fAuNCs-BSA. (A–C) Fluorescence images of Hoechst stained astrocytes: (A) NT, (B) BSA [1 mM], and (C) fAuNCs-BSA [1 mM]- treated cells captured at 3 DIV. Red and blue signals come from the fAuNCs-BSA treated cells and the stained nuclei. Scale bar is 25 µm. (D,E) Averaged fluorescence emission spectra obtained at excitation wavelengths of (D) 360 nm and (E) 480 nm for NT (black traces), BSA [1 mM] (gray traces), and fAuNCs-BSA [1 mM] (red traces) treated cells at 3 DIV (right panels, cells (+)), compared with saline solutions of BSA [1 mM] (gray traces) and fAuNCs-BSA [1 mM] (red traces) (left panels, cells (-)).

studies, the difference in nanocluster localization could depend on i) size [28, 32], ii) aggregation [18], iii) the presence/absence and the structure of templating protein (e.g., BSA) [16], and iv) genotypic and phenotypic differences between cell lines used [21]. Collectively these data confirm that fAuNCs-BSA internalize into the cell, influencing the morphological properties of astrocytes, with no inflammation or oxidative stress effects, highlighting their promising utility in biolabeling and imaging of astrocytes.

2.3 | Effect of fAuNCs-BSA on Electrophysiological Properties of Astrocytes

To examine the effect of the treatment with [1 mM] fAuNCs-BSA on ion channels, which are important in astrocytes for their physiology both in vitro and in vivo [1–6], we performed single-cell whole-cell patch-clamp measurements on NT (Figure 5A) and fAuNCs-BSA-treated astrocytes after 3 DIV (Figure 5B) and 2 weeks (14 DIV) from incubation with [1 mM] of fAuNCs-BSA (Figure S5 A,B). The cells were voltage clamped at a holding potential (V_h) of −60 mV and then stimulated with a voltage ramp from −120 to 60 mV (inset, Figure 5A), using standard intracellular and extracellular saline solutions (see Materials and Methods), to record whole-cell currents. The ramp current amplitude was recorded and passive membrane properties were calculated (Table 1). The average resting membrane potential (Vmem) of NT cells was −30 ± 5 mV. This value is consistent with those previously reported for primary astrocytes cultured on different flat and standard substrates [33–38]. The Vmem was not significantly different in fAuNCs-BSA-treated cells from

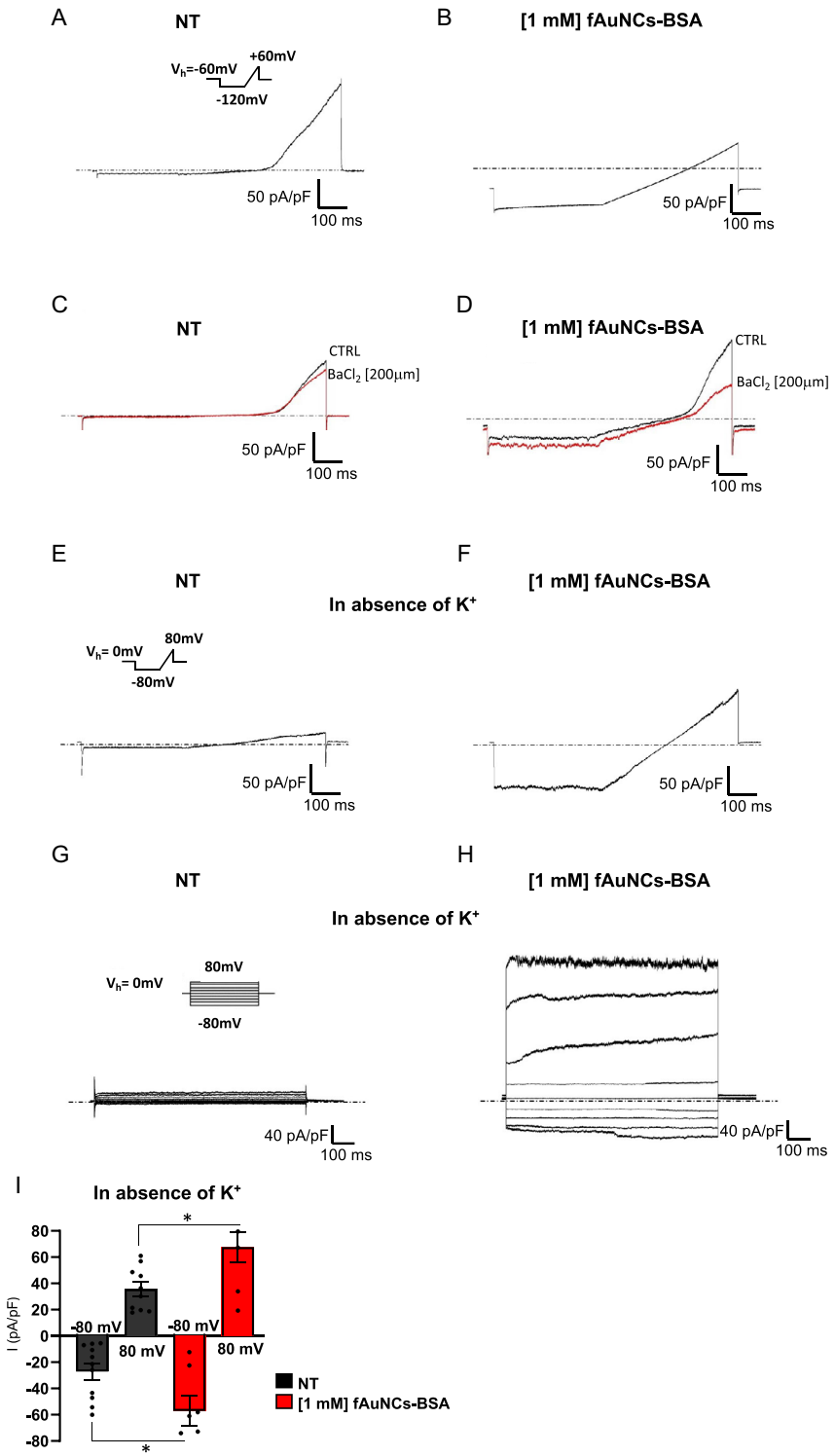

FIGURE 5 | Effects of fAuNCs-BSA on astrocytic whole-cell currents. (A–D) Typical current traces recorded stimulating astrocytes with a voltage ramp protocol (inset to panel A) from −120 to + 60 mV (500 ms) with (A,C) $V_h = -60$ mV, in NT astrocytes, (B,D) fAuNCs-BSA [1 mM] treated astrocytes after 3DIV, before (C,D black traces) and after (C,D, red traces) the application of $BaCl_2$, inhibitor of Kir4.1 (E–H) Effects of fAuNCs-BSA on bioelectrical properties of astrocytes when K^+ currents were inhibited using internal CsCl solution. (E,F) Current traces recorded stimulating astrocytes with the voltage ramp protocol shown in the inset from V_h −80 to + 80 mV (500 ms), in (E) NT and (F) fAuNCs-BSA [1 mM] treated astrocytes. (G,H) Representative current traces of voltage-activated current recorded in (G) NT and (H) fAuNCs-BSA-treated astrocytes. Astrocytes were voltage clamped at the holding potential (V_h) of 0 mV, and a family of voltage steps were delivered from −80 to + 80 mV, with an increment of 20 mV for each step with a duration of 400 ms (see inset in (G)). (I) Bar plot reporting the averaged value for the peak current density at −80 and + 80 mV in NT and fAuNCs-BSA-treated astrocytes ($N = 12$ for NT, $N = 9$ for fAuNCs-BSA [1 mM], N = number of recorded cells). Data are reported as mean ± SE. Statistical significance was calculated via one-way ANOVA with Bonferroni post-test. *: $p < 0.05$, **: $p < 0.01$, ***: $p < 0.001$. Statistical difference was observed between NT and fAuNCs-BSA [1 mM] in I (pA/pF) (−80 mV) ($p = 0.02$) and in I (pA/pF) (+80 mV) ($p = 0.013$).

NT after 3 DIV and 14 DIV. However, a substantial decrease in the input resistance (Table 1, IR) values was observed in NT astrocytes compared to the one recorded in fAuNCs-BSA cells at 3 DIV and 14 DIV, respectively (Table 1). Accordingly, the average of specific conductance (Table 1, SG) values recorded at −60 mV (Table 1) indicated a progressive significant increase of SG in fAuNCs-BSA-treated astrocytes. The average of the calculated capacitance (Table 1,C) was not considerably different between NT and fAuNCs-BSA-treated cells at 3 DIV, but it was at 14 DIV (Table 1). Given that the capacitance is correlated with the cell surface area, the data is consistent with the one expected for differentiated cells, which displayed a higher number of long extended processes that increase the overall cell surface area [33–38].

Interestingly, the ramp currents recorded in [1mM] fAuNC-BSA treated cells at 3 DIV and 14 DIV (Figure 5B) displayed inward and outward profiles, compared to currents recorded in NT cells (Figure 5A), that displayed only outward rectifying whole-cell conductance, as described previously [33–38]. Accordingly, the maximal current density measured at −120 and 60 mV was significantly higher in absolute value for [1 mM] fAuNCs-BSA-treated astrocytes compared to NT cells (Table 1).

It should be noted that the effect of fAuNCs-BSA on the functional properties of astrocytes was long-lasting. The magnitude of inward and outward current densities (Table 1, IMAX −120 mV; IMAX + 60 mV) and the input resistance (Table 1, IR) were significantly higher in [1 mM] fAuNCs-BSA-treated cells, while the SG significantly decreased over time. Overall, the data are consistent with effects expected from long-term modulation of cellular function.

Previous studies have reported that the interaction of astrocytes with nanostructured films or nanoparticles, such as hydrotalcite films [33, 34], gold-coated silicon nanowires [47], or graphene nanoflakes [36], induced astroglial cells differentiation, accompanied by an upregulation of K^+ channel (Kir4.1) [33, 34, 36–38], or by Chloride currents that could be mediated in differentiated astrocytes by ClC channel protein [35, 48] and or by Volume Regulated Anion Conductance mediated by LRCC8-A [34, 48, 49].

The ramp current profiles recorded at 3 DIV in [1 mM] fAuNCs-BSA-treated cells (Figure 5A,B) do not resemble the canonical biophysical profile of astroglial Kir4.1 channels, which is typically characterized by a strong inward rectifying behavior [33, 34, 36–38]. The addition of submillimolar concentrations of $BaCl_2$ (200 μM, Figure 5C,D, red traces) does not significantly alter inward currents induced by the treatment with [1 mM] fAuNCs-BSA. These observations suggest that the currents induced by fAuNCs-BSA are unlikely to be mediated by classical Kir4.1 channels, but rather may involve other conductance or mechanisms affecting membrane permeability.

To verify the influence of anionic conductance on the whole-cell current induced by fAuNCs-BSA and to avoid interference of the K^+ currents in the recording, we performed patch-clamp experiments where K^+ was omitted from the intracellular solution and replaced with cesium (CsCl) [34, 49] (Figure 5E–H). The NT and [1 mM] fAuNCs-BSA were voltage clamped at the holding potential (V_h) of 0 mV, next to the astrocytic zero-current

TABLE 1 | Passive electrophysiological properties of fAuNCs-BSA-treated astrocytes. Statistics of passive electrophysiological properties of NT and fAuNCs-BSA [1mM] treated astrocytes at 3DIV (for NT (3 DIV), $N = 11$ and for fAuNCs-BSA [1mM] (3 DIV), $N = 17$), and of NT and fAuNCs-BSA [1mM] treated astrocytes at 14 DIV (for NT (14 DIV), $N = 3$ and for fAuNCs-BSA [1mM] (14 DIV), $N = 6$), N = number of recorded cells. Data are reported as mean ± SE. Statistical significance was calculated via one-way ANOVA with Bonferroni post-test. *$p < 0.05$, **$p < 0.01$, ***$p < 0.001$. Statistical difference was observed between NT (3 DIV) and fAuNCs-BSA [1mM] (3 DIV) for I MAX (−120) ($p = 0.014$), I MAX (+60) ($p = 0.04872$), IR ($p = 9.1\ 10^{-7}$), SG ($p = 7.8\ 10^{-5}$). No statistical difference was observed between NT (3 DIV) and fAuNCs-BSA [1mM] (3 DIV) for C ($p = 0.8$), Vmem ($p = 0.6$). Statistical difference was observed between NT (14 DIV) and fAuNCs-BSA [1mM] (14 DIV) for I MAX (−120) ($p = 4.6\ 10^{-5}$), I MAX (+60) ($p = 3.7\ 10^{-6}$), IR ($p = 3.6\ 10^{-4}$), SG ($p = 0.09$). No statistical difference was observed between NT (14 DIV) and fAuNCs-BSA [1mM] (14 DIV) for C ($p = 0.06$), Vmem ($p = 0.5$). Statistical difference was observed between NT (3 DIV) and NT (14 DIV) for I MAX (−120) ($p = 0.03$), I MAX (+60) ($p = 0.005$), IR ($p = 6.5\ 10^{-7}$), SG ($p = 5.2\ 10^{-4}$). No statistical difference was observed between NT (3 DIV) and NT (14 DIV) for C ($p = 0.3$), V_{mem} ($p = 0.3$). No statistical difference was observed between fAuNCs-BSA [1mM] (3 DIV) and fAuNCs-BSA [1mM] (14 DIV) for C ($p = 0.1$), Vmem ($p = 0.7$), I MAX (−120) ($p = 0.4$), I MAX (+60) ($p = 0.2$), IR ($p = 0.08$), SG ($p = 0.2$).

	C, pF	Vmem, mV	I MAX, −120, pA/pF	I MAX, + 60, pA/pF	I R, M Ω	SG, nS/pF
NT, 3 DIV N = 11	25 ± 2.7	−30.5 ± 5.1	−6.2 ± 0.9	37.7 ± 17.6	355 ± 47	0.14 ± 0.01
fAuNCs-BSA [1 mM], 3 DIV N = 17	24 ± 2.4	−22.4 ± 11.3	−112 ± 23**	82 ± 16*	44 ± 6***	1.2 ± 0.2***
NT, 14 DIV N = 3	20 ± 2	−22 ± 7	−4 ± 0.5	18 ± 20	299 ± 38	0.05 ± 0.01
fAuNCs-BSA [1 mM] 14 DIV N = 6	36 ± 7	−29 ± 7.4	−217 ± 40***	150 ± 22***	21 ± 3.6***	1.9 ± 0.3***

potential of Chloride (Cl^-) and stimulated with voltage ramps ranging from −80 to + 80 mV (Figure 5E–F). Whole-cell membrane conductance recorded in extracellular CsCl saline (Figure 5E,F) show a dramatic increase of the anionic current with a pronounced outward rectification profile in the case of [1 mM] fAuNCs-BSA-treated astrocytes (Figure 5F). Accordingly, [1 mM] fAuNCs-BSA astrocytes exhibit a significant increase in the magnitude of the maximal whole-cell current density (recorded at −80 and + 80 mV), recorded at the steady state, compared to NT astrocytes (Figure 5I).

To analyze the biophysical properties of Cl^- conductance, cells were stimulated by a voltage protocol consisting in a family of voltage-step (inset to Figure 5G) from −80 to + 80 mV, incremented by 20 mV every 10 sec. Consistent with the biophysical profile of chloride ion channels characterized in primary astrocytes [34, 35, 48, 49] in fAuNCs-BSA-astrocytes, the currents activate instantaneously at all voltages (Figure 5H), compared to NT astrocytes (Figure 5G) where the inward and outward currents were negligible. The rectification, voltage, and time-dependent profile suggest the involvement of VRAC [34, 48, 49]. However, the time dependence observed in response to the voltage ramp protocols did not show the fast deactivation observed in response to a voltage above 40 mV, typical of VRAC [34, 48, 49]. It is important to point out that differentiated astrocytes could express additional chloride channel conductance mediated by ClC-2 [35, 48]. The latter is activated upon membrane hyperpolarisation, presenting a slow time-course, inward rectifying current [35]. Thus, it is plausible that the observed current is a hybrid or concurrent activation of both VRAC and ClC, previously characterized in astrocytes [34, 35, 48, 49]. Electrophysiological analyses demonstrate that [1 mM] fAuNCs-BSA-treatment impacts on the Cl^- channel dynamics and whole-cell membrane conductance. Notably, the immunofluoresent expression levels of LRRC8-A, the protein forming the pore of VRAC, was not altered by the treatment with [1 mM] fAuNCs-BSA (Figure S6). It is highlighted that increase in VRAC current and more general an increased chloride conductance is abundantly reported to be engaged in differentiation processes, occurring in different cell types [50, 51], including astrocytes [34, 35, 52]. In this respect, the data further supports that [1 mM] fAuNCs-BSA induces astrocytes morphological and functional differentiation. It is possible that astrocytes, sensing the different chemical compositions due to [1mM] fAuNCs-BSA, rearrange their volume distribution and ion spatial buffering capability, resulting in a more efficient water and ion permeability and consequent volume regulation [34]. As an alternative mechanism, VRAC is also known to mediate the release of gliotransmitters [7]. Thus, the upregulation of VRAC/Chloride conductance might increase the release of molecules that, in turn, impact the differentiation of astrocytes and induce further modification of their functional properties. Future studies using inhibitors of these receptor pathways will likely clarify this issue.

2.4 | Effects of fAuNCs-BSA on Cell Volume Regulation and Calcium Dynamics in Astrocytes

Given the importance of astrocytes water and cell volume regulation in the brain [1, 2] and the role of chloride conductance in these astrocytic processes [34, 35, 51], we next explored the effects of fAuNCs-BSA treatment on astrocyte water permeability and cell volume regulation properties (Figure 6A,B). No significant differences were observed in the time constants (τ) of cell swelling or shrinkage between NT and [1mM] fAuNCs-BSA-treated astrocytes, indicating comparable water transport kinetics (Figure 6A). of In contrast, exposure to both hypotonic and hypertonic gradients significantly affected the magnitude of cell volume changes in NT and [1 mM] fAuNCs-BSA-treated astrocytes (Figure 6B). Considering the key role of AQP4 in the water permeability and cell volume regulation in astrocytes [1, 2], we performed western blot analyses and relative quantification (Figure S7 E–F) to get further insights into the effect of fAuNCs-BSA treatment on AQP4 expression. It is observed that despite the higher increase in the extent of volume amplitude over an isotonic gradient, the expression levels of AQP4 in fAuNCs-BSA-treated cells were not significantly different (Figure S7 E–F).

Astrocytes are capable of sensing and responding to different extracellular chemophysical stimuli (such as osmotic and ion gradient, temperature, mechanical stimulus, neurotransmitters) [1–6, 53, 54] by changes in their concentration of free intracellular calcium ($[Ca^{2+}]_i$).

Considering the importance of calcium signaling in astrocytes physiology and in their interaction with neurons [1, 2, 6], we performed calcium imaging experiments to understand the effect of [1 mM] fAuNCs-BSA treatment on $[Ca^{2+}]_i$. Astrocytes were loaded with the calcium indicator X-Rhod-1-AM [1 μM]. Time-lapse images of fluorescent astrocytes were recorded with a sampling rate of 2 Hz. Changes over time in fluorescence intensity ($\Delta F_t/F_{t0}$), which are directly related to $[Ca^{2+}]_i$ variations, were analyzed in the cell and reported as representative curves (Figure 6C,D). In control saline solution (CTRL), fast activating and sustained increase in $[Ca^{2+}]_i$ was observed in fAuNCs-BSA treated astrocytes (Figure 6D) compared to NT cells (Figure 6C). The magnitude of the $[Ca^{2+}]_i$ was significantly higher in [1 mM] fAuNCs-BSA-treated astrocytes compared to NT cells (Figure 6E), while the percentage of cells with a $[Ca^{2+}]_i$ above the threshold was comparable (Figure 6F). We performed analyses of the temporal dynamics of astrocytes $[Ca^{2+}]_i$, which reveals that, in control saline, the onset of the calcium signal (Figure S7 A), the time to peak (Figure S8 B) and the number of oscillations (Figure S8 C) were comparable between NT and [1 mM] fAuNCs-BSA-treated astrocytes.

The pharmacological analyses revealed that the large and long-lasting response of fAuNCs-BSA-treated cells was not inhibited by the removal of Ca^{2+} from the extracellular solution (Figure 6E, blue bar), but it was almost completely suppressed by inhibition of the Inositol-3-Phosphate-Receptor (IP3Rs) pathway, which is involved in astrocyte communication and response to external stimuli, such as mechanical and osmotic ones (Figure 6E, orange bar) [6, 7, 53]. Notably, the addition of RN-1734 [10 μM], a selective inhibitor of Transient Receptor Potential Vanilloid Channels (TRPV4) (Figure 6D, RN, green traces), significantly inhibited the magnitude of the Ca^{2+} response (Figure 6E), but not its dynamics nor the percentage of the responding cells (Figure S8)

It is important to note that the tail of the absorption spectrum of fAuNCs-BSA overlaps with the wavelength of the LED ($\lambda_{ex} = 535$) used to photoexcite the X-Rhod calcium fluorophore [16]. Thus, it is plausible that the observed effects are caused by a thermal and/or photonic effect due to the excitation of the metal nanoclusters. The latter may activate TRPV4, a polymodal, thermally-activated calcium channel expressed in astrocytes in vitro and in vivo [9, 53–55]. Notably, the expression of TRPV4 was

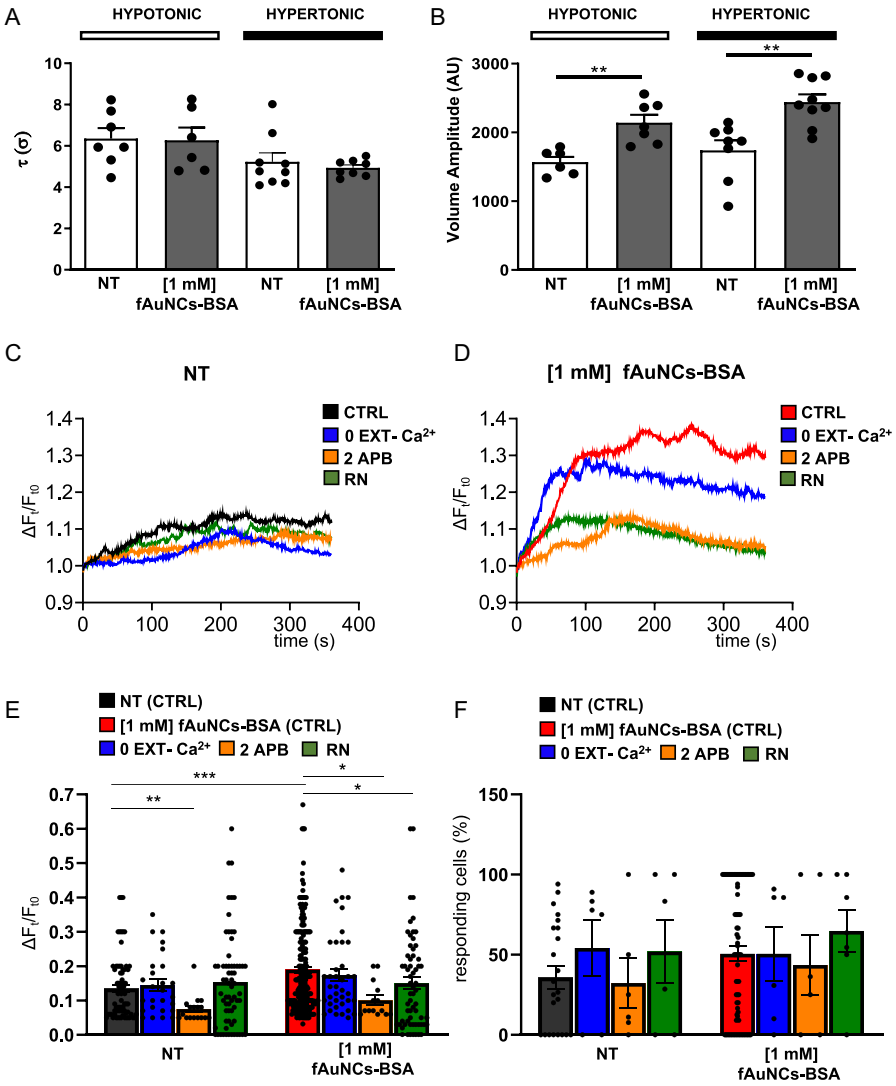

FIGURE 6 | Effects of fAuNCs-BSA on cell volume regulation and calcium dynamics in astrocytes. (A,B) Comparison of water transport properties of NT and fAuNCs-BSA astrocytes during the swelling and the shrinking phase. Quantitative analysis of (A) the cell swelling time constants (τ) and of the shrinking and (B) the extent of volume recovery (%) I at the applied hypertonic gradients. For time constant (τ) in Hypotonic condition, $n = 7$ for NT and $n = 6$ for fAuNCs-BSA[1 mM]. For time constant (τ) in Hypertonic condition, $n = 9$ for NT and $n = 8$ for fAuNCs-BSA[1 mM]. For Volume Amplitude in Hypotonic condition, $n = 6$ for NT and $n = 7$ for fAuNCs-BSA[1 mM]. For Volume Amplitude in Hypertonic condition, $n = 8$ for NT and $n = 9$ for fAuNCs-BSA[1 mM] (n = number of measurements). Data are reported as mean ± SE. One-way ANOVA and Newman-Keuls Multiple Comparison Test were performed. ***$p < 0.0001$; **$p < 0.001$; *$p < 0.01$. (C,D) Representative traces of calcium imaging experiments performed on (C) NT cells and (D) fAuNCs-BSA [1 mM] treated cells. The traces represent the dynamic variation of the intracellular calcium over time, measured in standard extracellular solution (CTRL, black trace for NT and red trace for fAuNCs-BSA [1 mM]), and under pharmacological treatment by removing calcium from the extracellular solution (0 EXT Ca^{2+}, blue traces) and upon the exposition to 2-aminoethoxydiphenyl borate [100 μM] (2APB, inhibitor of IP_3, orange traces) and to RN-1734 [10 μM] (RN, inhibitor of TRPV4, green traces). (E,F) Bar-dot graphs representative of the statistical analysis of calcium imaging experiments conducted on astrocytes, showing the (E) average values of variation of fluorescence and (F) the percentage of responding cells, in NT and treated cells. For CTRL condition, $n = 75$, $N = 9$ for NT and $n = 230$, $N = 9$ for fAuNCs-BSA [1 mM]. For 0 EXT Ca^{2+} condition, $n = 26$, $N = 3$ for NT and $n = 39$, $N = 3$ for fAuNCs-BSA [1 mM]. For 2APB condition, $n = 17$, $N = 3$ for NT and $n = 14$, $N = 3$ for fAuNCs-BSA [1mM]. For RN condition, $n = 48$, $N = 3$ for NT and $n = 43$, $N = 3$ for fAuNCs-BSA [1 mM] (n = number of cells, N = number of independent experimental trials). Data are reported as mean ± SE. Statistical significance was calculated via one-way ANOVA with Bonferroni post-test. *: $p < 0.05$, **: $p < 0.01$, ***: $p < 0.001$. Number of experimental trials, replicates and cells recorded for each condition tested is reported in Table S1. Statistical difference was observed in $\Delta F_t/F_{t0}$ between NT CTRL and NT + 2APB ($p = 0.009$), between fAuNCs-BSA [1 mM] CTRL and fAuNCs-BSA [1 mM] + 2APB ($p = 0.013$) and between fAuNCs-BSA [1 mM] CTRL and fAuNCs-BSA [1 mM] + RN ($p = 0.04$). Statistical difference was observed in $\Delta F_t/F_{t0}$ between NT CTRL and fAuNCs-BSA [1 mM] CTRL ($p = 0.0008$). No statistical difference was observed in $\Delta Ft/F_{t0}$ between NT CTRL and NT 0 EXT-Ca^{2+} ($p = 0.6$), between NT CTRL and NT + RN ($p = 0.3$), and between fAuNCs-BSA [1 mM] CTRL and fAuNCs-BSA [1 mM] 0 EXT-Ca^{2+} ($p = 0.47$). No statistical difference was observed in responding cells (%) between NT CTRL and NT 0 EXT-Ca^{2+} ($p = 0.26$), between NT CTRL and NT + 2APB ($p = 0.8$), and between NT CTRL and NT + RN ($p = 0.3$). No statistical difference was observed in responding cells (%) between fAuNCs-BSA [1 mM] CTRL and fAuNCs-BSA [1 mM] 0 EXT-Ca^{2+} ($p = 0.99$), between fAuNCs-BSA [1mM] CTRL and fAuNCs-BSA [1 mM] + 2APB ($p = 0.69$), and between fAuNCs-BSA [1mM] CTRL and fAuNCs-BSA [1 mM] + RN ($p = 0.4$). No statistical difference was observed in responding cells (%) between NT CTRL and fAuNCs-BSA [1 mM] CTRL ($p = 0.11$).

not altered in NT and [1 mM] fAuNCs-BSA-treated astrocytes (Figure S6).

Collectively, these findings show that treatment with [1 mM] fAuNCs-BSA induces morphological differentiation of astrocytes in vitro, which is accompanied by alteration of functional features, including chloride currents, water permeability, and calcium signaling, which are also critical for the physiology of astrocytes in vivo (Figure S9A) [1–7].

2.5 | Photoexcitation of fAuNCs Nanobiophotonics Probes Alters Astrocytes Whole-Cell Potassium Current through a Thermal Effect

To verify whether LED photostimulation of fAuNCs-BSA affects/modulates whole-cell channel conductance or modify its biophysical properties, we performed patch-clamp experiments in whole-cell configuration on NT and fAuNCs-BSA treated astrocytes, applying the same ramp protocols described above using the exact solution protocols to isolate potassium or chloride currents, and recording the ramp currents during stimulation with light ($\lambda_{ex} = 450$ nm), that was applied when the current reached the steady state. Whole-cell membrane conductance was measured in the same conditions for NT and fAuNCs-BSA treated cells. The response to the photoillumination in the presence of K^+ in the intracellular and extracellular solution is shown in the I–V plots of Figure 7A,B. As can be noticed, the normalized residual current shows a decrease of about 30% in the outward current in [1 mM] fAuNCs-BSA-treated cells (Figure 7B) when the light is switched on, but no significant differences are observed in NT astrocytes (Figure 7A). In Figure 6C,D, we report the bar dot plots of the peak current values, calculated as the ratio between the peak currents in standard conditions (CTRL, black line) and during photostimulation (red line) for NT (gray bars) and [1 mM] fAuNCs-BSA (yellow bars)-treated astrocytes. The measurements were performed at −120 and + 60 mV (in the presence of K^+) (Figure 7C) and at −80 and + 80 mV (removing K^+ from extra- and intracellular solutions) (Figure 7D). Here, we observe a significant difference in the peak current expression, due to the photostimulation in presence of K^+ (Figure 7C). No difference has been observed when K^+ is absent (Figure 7D).

Ongoing and future analyses are still devoted to understand which cationic and anion currents elicited by specific K^+ and Cl^- currents are implicated in this mechanism.

It is interesting to note that the treatment fAuNCs-BSA upregulates chloride current over short (3DIV) and long-term (14 DIV), while acute photostimulation downregulates the K^+ conductance.

Previous studies have shown that whole-cell cationic current of astrocytes can be modulated by photostimulation at the organic optoelectronic interface [56]. Recently, Borrachero-Conejo et al. reported that pulsed infrared light (IR) can modulate astrocyte

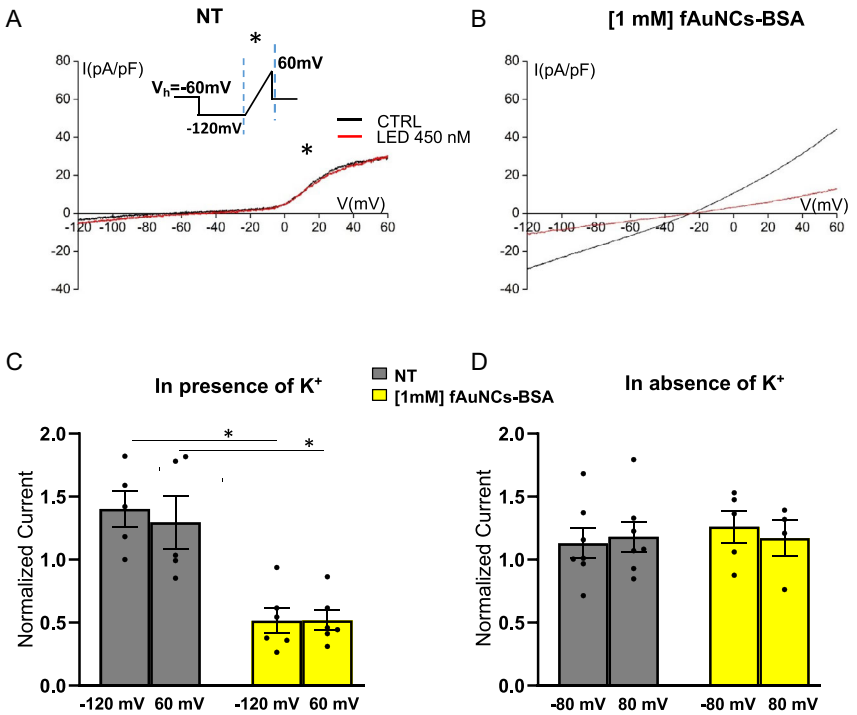

FIGURE 7 | Photoexcitation of fAuNCs alters astrocyte whole-cell potassium current. (A,B) Current traces from I/V plot of (A) NT astrocytes and (B) fAuNCs-BSA [1 mM] treated astrocytes in standard condition (black line, CTRL) and after LED stimulation (red line, photostimulation) in presence of potassium in the intracellular and extracellular solution. (C,D) Histogram reports the mean value of the peak current ratios for NT (gray bar) and for fAuNCs-BSA treated astrocytes (yellow bar) at −120 mV and + 60 mV (C) and −80 mV and + 80 mV (D). In presence of potassium, $N = 5$ for NT and $N = 6$ for fAuNCs-BSA [1 mM]. In absence of potassium, $N = 7$ for NT and $N = 5$ for fAuNCs-BSA [1 mM] (N = number of recorded cells). Data are reported as mean ± SE. Statistical significance was calculated via one-way ANOVA with Bonferroni post-test. *: $p < 0.05$, **: $p < 0.01$, ***: $p < 0.001$. Statistical difference was observed between NT and fAuNCs-BSA [1 mM] (in presence of K^+) in Normalized current (−120 mV) ($p = 5.72\ 10^{-4}$) and in Normalized current (+60 mV) ($p = 0.005$). No statistical difference was observed between NT and fAuNCs-BSA [1 mM] (in absence of K^+) in Normalized current (−80 mV) ($p = 0.47$) and in normalized current (+80 mV) ($p = 0.95$).

functions through variations in intracellular Ca^{2+} and water dynamics [57]. These findings have been attributed to photonic and/or thermal effects induced by the external stimuli. Therefore, we hypothesize that our observation of the photoinduced changes in astrocyte cell electrical activity might be a consequence of photothermal effect in the presence of fAuNCs, in analogy with what has been reported for larger Au nanoparticles [58, 59].

To examine our hypothesis, we performed diamond nitrogen-vacancy (NV) center thermometry. The technique relies on the fact that the fluorescence emission of a NV is associated with its spin properties and can be manipulated with microwave pulses, showing a sharp decrease of the intensity at a resonance frequency which is temperature dependent [60]. The method consists of the optical detection of the spin resonance (hence called optically detected magnetic resonance (ODMR)). It has been previously used to perform precise temperature measurements in living cells with high spatial resolution [61, 62]. Figure 8 shows our experimental setup, made of a fluorescence microscope excited with laser light of wavelength, $\lambda = 532$ nm and power = ≈1 mW, coupled with a microwave source and antenna and controlled with computer software. In Figure 8B, we plot a typical ODMR spectrum recorded on a film of NV-rich fluorescent nanodiamond (ND) (Merck, size ≈100 nm), averaging the signal of an area approximatively equal to $100 \times 100\ \mu m^2$. We then deposited fAuNCs-BSA at different concentrations (namely 0.1, 1, 10 mMol l^{-1}) onto the ND film and recorded the corresponding spectra. In Figure 8C, we plot the fluorescence intensity vs. microwave frequency for the films containing only NDs and with the Au nanoclusters (fAuNCs-BSA), the latter showing a detectable shift of the resonance toward lower frequency values corresponding to higher temperatures. We repeated similar measurements on 12 different zones for each sample. We averaged the extracted center peak frequencies, showing the results in Figure 8D, where the resonance frequency shift is transformed in temperature difference, using the relation $f_0 \approx -74\ KHz\ K^{-1}\ \Delta T$ [63]. It is observed that the film average temperature increases when the quantity of fAuNCs increases, thus confirming our hypothesis that the Au cluster may locally induce a heating effect when illuminated (in this case by the laser used to perform the temperature sensing). It is important to underline that our estimated temperature difference is an average effect, while at the cluster site, the actual increase is likely larger [61]. It is possible that such a photothermal effect can also play a role in the activation of the thermally sensitive calcium channels, expressed in astrocytes, which are responsible for the calcium dynamic described in the previous section (Figure S9B).

3 | Conclusions

In summary, we characterized fAuNCs-BSA as biocompatible nanoprobes that can be naturally embedded in astroglia cells. The treatment of primary cortical astrocytes with fAuNCs-BSA induces a dose-dependent morphological differentiation by promoting a significant cytoskeleton rearrangement and "stellation" without overexpression of GFAP, demonstrating no inflammatory reaction. The morphological differentiation is accompanied by the up-regulation of whole-cell chloride conductance, water transport, and calcium signaling. These findings open the way to functional regulation of astrocyte ion channels in vitro by

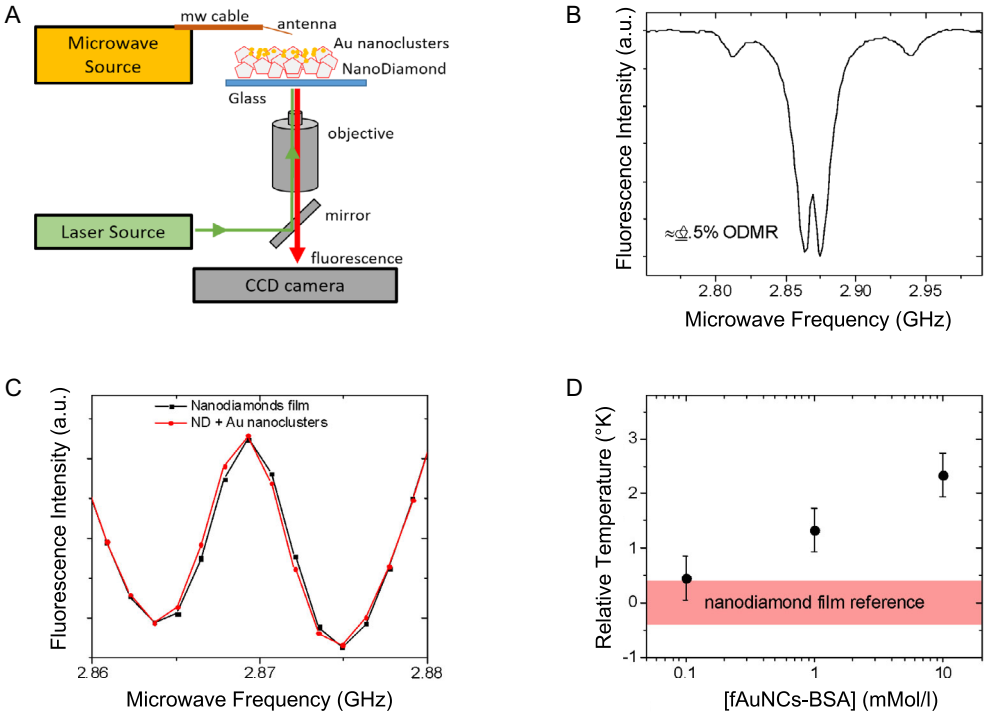

FIGURE 8 | fAuNCs-BSA may locally induce a photothermal effect. (A) Experimental setup used for ODMR measurements, consisting of a fluorescence microscope excited with laser light (532 nm) and microwave source and antenna to excite the sample. (B) Typical ODMR spectrum recorded on a film of NV-rich fluorescent nanodiamonds. (C) Fluorescence intensity vs. microwave frequency for the films containing ND (black line) and ND + fAuNCs-BSA (red line). (D) Relative temperature difference, calculated from the shift of the resonance frequency (see text), when the concentration of fAuNCs deposited on the ND film is varied.

applying nanotools such as metal nanoclusters. Finally, we demonstrate that the photoexcitation of fAuNCs-BSA-treated astrocytes alters the expression of anionic and cationic currents and the dynamics of basal intracellular calcium, likely due to a photothermal effect, as corroborated using NVc thermometry.

In a broader perspective, fAuNCs can be used as i) nanotools to morphologically differentiate astrocytes in vitro; ii) photonic probe to monitor and image astrocyte dynamics; iii) photonic sensor to modulate the main cellular conductance acutely and over time; iv) quantum systems to probe the role of astrocytic biophysical properties in brain function and dysfunction. Finally, the combined use of fAuNCs and other photonic nanoprobes, such as diamond NV centers, for biosensing offers novel opportunities that can be leveraged to probe glial and potentially other neuronal cell morphological/functional properties [64–69]. It should be noted that astrocyte ion channel expression and electrical properties can vary across brain regions and species. Recognizing this variability provides a valuable opportunity for future studies to compare the effects of fAuNCs on astrocyte properties across different regions and experimental models, which will further enhance our understanding of the broader impact of nanocluster on cellular function [70, 71]. From a future perspective, the potential of employing fAuNCs-based nanoplatform to sense, modulate and drive the functions of brain astrocytes could lead the development of advanced theranostic nanotechnologies, simultaneously integrating glial-targeted diagnosis and therapy approaches to improve the detection and treatment of many currently incurable neurological disorders. Finally, with the use of nanodiamond this workset the scene for combining quantum sensing and photonic probes to interface, study and dialogue with astrocytes.

4 | Materials and Methods

4.1 | Preparation of Fluorescent Gold Nanocluster (fAuNCs) Solutions and Cell Treatment

fAuNCs-BSA were synthesized by adapting the methodology from Xie et al. [16, 18] 5 ml of BSA solution (20 mg/ml) was mixed with 5 ml of gold salt solution (10 mM HAuCl4 $3H_2O$) and stirred thoroughly for 2 min, followed by the addition of 0.5 ml of NaOH (1 M) and further stirring for 2 min. Finally, the solution was incubated at room temperature for 24 h. Samples were lyophilized and stored at 4°C.

4.2 | DLS and SZP

DLS and SZP analysis have been performed using a NanoBrook Omni on freshly prepared solutions of fAuNCs-BSA in pure water at a concentration of 1 mM.

4.3 | Rat Cortical Astrocyte Culture Preparation, Maintenance, Plating, and Treatment

Primary astrocyte cultures were obtained from newborn Sprague Dawley rat pups (postnatal days P 0–2), following a previously established protocol [33, 35]. All the experimental procedures complied with the Italian regulations on laboratory animal protection, and were approved by the bioethical committees of the University of Bologna and of the Ministry of Health (protocol number 1138/2020-PR) and supervised by Veterinary Commission of the University of Bologna for animal care and comfort.

In short, neonatal cerebral cortices were dissected, dissociated, and plated in Dulbecco's Modified Eagle Medium (DMEM)+ GlutaMAX (Thermo Fisher Scientific) supplemented with 15% fetal bovine serum (FBS, Sigma Aldrich) and antibiotics, then cultured for 2 weeks at 37°C, 5% CO_2, with medium changes every 2 days and removal of microglial cells by gentle agitation. Once confluent, astrocytes were detached with trypsin-EDTA (Thermo Fisher Scientific), and replated on poly-D-lysine (PDL, Sigma Aldrich)-coated glass coverslips. Additional details are reported in previous studies [33, 38].

Astrocytes were seeded at a density of $5–7 \times 10^3$ per sample in 10% FBS—supplemented culture medium. 24 h after replating, cells were treated with fAuNCs-BSA before performing single experiments. For in vitro experiments, 0.004 g of HAuCl4 and of fAuNCs-BSA powder was dispersed in 1 ml of phosphate buffered saline (PBS) and dissolved in 9 ml of 10% FBS culture medium. 1 min of sonication was performed to obtain [1 mM] of HAuCl4 and fAuNCs-BSA in solution. Cells were incubated for 24 h with the different concentrations of fAuNCs-BSA (0.1 mM, 1 mM) or with [1 mM] HAuCl4 solutions in water injected incubator at 37°C and 5% CO_2 and then rinsed with PBS prior to experiments.

4.4 | Fluorescein Diacetate/Hoescht Live/Dead Assay and Confocal Microscopy

The viability of fAuNCs-BSA-treated astrocytes was analyzed by the fluorescein diacetate assay (FDA, 5 mg/ml) to mark viable cells and Hoechst 33 342 (Thermo Fisher Scientific) to stain cellular nuclei, diluted in PBS. After 5 min of incubation with FDA/Hoechst 33 342 solution at room temperature (22°C–24°C), astrocytes were rinsed with PBS and observed using a Fluo Spin Up upright CREST confocal microscope (Crisel Instruments, Rome, Italy) equipped with 20X and 40X water immersion objectives [33].

Confocal images of FDA/Hoescht-stained astrocytes (10–15 fields of 0.3×0.3 mm per sample) were acquired with 20X and 40X water immersion objectives. Living cells (green fluorescent) and nonliving (blue stained but not green stained) were counted and the cell density (number of cells/ mm^2) was evaluated across the following time points: 24 h, 3 days after the fAuNCs treatment (days in vitro, DIV), 14 DIV, and 21 DIV. Data from at least from three different experiments, each in triplicate, were analyzed using ORIGIN-PRO (Microcal) and Graphpad [33, 56].

4.5 | Reactive Oxygen Species (ROS) 2′, 7′-Diclorofluorescina Diacetate (DCFH-DA) Assay

1×10^4 cells were seeded in Corning Costar 96-well black clear-bottom plates in 10% FBS-supplemented culture medium and grown at 37°C in 5% CO_2. After 6 h, cells were treated for 24 h with [1 mM] BSA or [1 mM] fAuNCs-BSA. The media was replaced with complete DMEM after 24 h of treatment. Intracellular reactive oxygen species (ROS) production was

assessed using 2′, 7′-diclorofluorescina diacetate (DCFH-DA). DCFH-DA enters cells and is hydrolyzed by esterases to nonfluorescent DCFH, which is then oxidized by intracellular ROS into fluorescent DCF. At 3DIV, i.e., 48 h after the end of the treatment with [1 mM] BSA and [1mM] fAuNCs-BSA, cells were rinsed and then incubated for 30 min with 25 μM DCFH-DA in 1% PBS at 37°C. Cells used as positive control were stimulated for 1 h at 37°C with Fenton's reagent (H_2O_2/Fe^{2+} 2 mM), an oxidant agent able to boost intracellular ROS levels. The DCF signal was measured as fluorescence intensity using a fluorescent microplate reader (PerkinElmer VICTORTM X3 Multimode Reader) with an excitation wavelength of 485 nm and an emission of 535 nm. Additional details can be found in previous studies [72, 73].

4.6 | Cell Differentiation Measurement

Differentiation induced by fAuNCs-BSA treatment was assessed using previously defined morphological criteria [33].

Astrocytes with elongated and star-like shapes were identified as differentiated cells, while polygonal astrocytes were considered undifferentiated cells. Specifically, a cell was classified differentiated if its vertical axis was at least twice the length of its horizontal axis [33, 34]. A series of confocal images (10–15 fields of 0.3×0.3 mm per sample) of FDA-stained astrocytes was acquired using an Fluo-Spin Up upright CREST confocal microscope (Crisel Instruments, Rome, Italy) equipped with 20X and 40X water immersion objectives and analyzed using Fiji ImageJ software.

Quantitative analysis was performed by counting differentiated and undifferentiated astrocytes among FDA-positive (viable) cells, imaged at 24 h, 3 DIV, 14 DIV, and 21 DIV. The proportion of differentiated cells was calculated as a percentage of the total viable cells population.

4.7 | Cell Viability Alamar Blue Assay

Alamar Blue (AB) assay was performed as previously reported [30, 33], to assess cell metabolic activity. On the day of the assay (3 DIV, 14 DIV, and 21 DIV), AB reagent was added directly to the culture medium (10% v/v) for each sample and incubated for 6 h. Then, 100 μl of AB-containing medium was transferred to a 96 multiwell plate, and fluorescence was measured (545 nm Ex/590 nm Em) using a Thermo Scientific Varioskan Flash Multimode Plate Reader. Reduced AB emission, which directly correlates with cell metabolic capability, was recorded at 590 nm.

4.8 | Mitochondria Staining

fAuNCs treated astrocytes were labeled with the live-cell staining dye MitoTracker Red CMXRo (Thermo Fisher Scientific), according to the manufacturer's protocol. Cells were loaded with MitoTracker Red CMXRo diluted in basal medium (250 nM), for 30–45 min at room temperature (22°C–24°C), rinsed, and imaged using a Fluo-Spin Up CREST Confocal Microscope (Crisel Instruments, Rome, Italy) with a 40X water immersion objective.

4.9 | STEM

Samples were fixed with cold 2.5% glutaraldehyde diluted in PBS for 48 h, rinsed and stained with osmium tetraoxide (OsO_4) for 1 h at room temperature to provide contrast while imaging. Next, each sample was rinsed three times with distilled water and dehydrated in ethanol (35%, 50%, 70%, 95%, and 100%, respectively). Then, cells were embedded in resin, incubated at 70°C, and sliced for TEM imaging. Images were taken with a JEOL JEM2100 at 5 kV, and 200 mesh copper grids with lacey carbon film were used for analysis.

4.10 | SEM Characterization

Astrocytes treated with fAuNCs-BSA were stabilized with 2.5% glutaraldehyde diluited in PBS at 4°C for 1 h, washed three times with PBS for 5 min each and stained with 1% Osmium tetra-oxide (OsO_4) for 1 h at room temperature. After staining, the samples were rinsed three times with distilled water and dehydrated through a graded ethanol series (50%, 75%, 95%, and 99%) [74, 75]

For imaging fAuNCs-BSA from cell media, media solutions from astrocytes treated with 1 mM fAuNCs-BSA (1 mM) were drop-cast onto glass coverslips and left them to dry.

Because of the presence of Au in the samples, they were not sputter-coated with Au before the observation.

Images were taken employing a Zeiss LEO 1530 FEG using a beam energy of 8 KeV.

4.11 | Characterization of Spectral Properties

Fluorescence emission spectra fAuNCs-BSA were acquired using a Varioskan Flash Multimode Plate Reader (Thermo Scientific). Samples were excited at 360 and 480 nm and fluorescence emission spectra were collected, in the range from 550 to 800 nm [16]. The spectra were obtained by normalizing the raw fluorescence values to the peak fluorescence intensity for each sample. The normalized fluorescence values at each wavelength point were analyzed and averaged, from three independent measurements for each condition. Photoemission spectra were recorded in presence and in absence of cells. A set of 5 spectra for each condition was analyzed.

4.12 | Electrophysiology

Whole-cell patch-clamp for current recordings was performed following previously established protocols [33–38]. Experiments were conducted in vitro after 24 h from the fAuNCs-BSA treatment of astrocytes. Whole-cell currents were recorded from single NT and [1 mM] fAuNCs-BSA-treated astrocytes. Cells immersed in extracellular solution were set at −60 mV after stepping to −120 mV (500 ms).

To isolate K^+ current from activated Cl^- currents, whole-cell recordings were performed in cultured astrocytes, as previously described [48, 49]. Accordingly, astrocytes were clamped at the holding potential (Vh) of 0 mV, close to the astrocytic zero-current potential, and stimulated with voltage ramps ranging from −80 to + 80 mV. Membrane currents were amplified using an Axopatch 200B amplifier and responses analyzed with pCLAMP 10 software. Additional

details regarding signal recording and processing are reported in previous studies [33–38].

Electrophysiological recordings were performed at room temperature (22°C–24°C). Current amplitude, resting membrane potential (Vmem) and capacitance (C) values were determined, according to previously defined methodologies [37, 38]. Patch-clamp experiments were also carried out to investigate the functional response of NT and fAuNCs-BSA treated ion channels in astrocytes in response to LED light photostimulation (450 nm), to verify whether LED affects/modulates anionic and cationic channel conductance or modify astrocyte biophysical properties or voltage- and time-dependence. The illumination protocol consists of the 300s of ramp and step recording, while the LED light was multipulse delivered every 0.5 s.

4.13 | Solutions and Chemicals

Chemical compounds and salts used for the experiments were of the highest purity grade (Sigma Aldrich). The standard bath solution used for both electrophysiological investigations and calcium microfluorometry experiments contained (mM): 140 NaCl, 4 KCl, 2 $CaCl_2$, 2 $MgCl_2$, 5 glucose, 10 HEPES, pH 7.4 with NaOH, and osmolarity adjusted to 315 mOsm with mannitol. The intracellular (pipette) solution comprised (mM): 144 KCl, 2 $MgCl_2$, 10 HEPES, 5 EGTA, pH 7.2 with KOH and osmolarity 300 mOsm.

To isolate chloride currents, K^+ was removed from extracellular or intracellular solution, and pipette solutions were replaced with cesium (Cs). The intracellular (pipette) solution contained (mM): 100 Cs gluconate, 26 $CsCl_2$, 2 $MgCl_2$, 10 TES, 1 EGTA, pH 7.2 with CsOH and osmolarity adjusted to 300 mOsm with mannitol.

Calcium-free extracellular saline (0 EXT-Ca^{2+}) contained (mM): 140 NaCl, 4 $MgCl_2$, 4 KCl, 0.5 EGTA, 10 HEPES, pH 7.4 with NaOH and osmolarity adjusted to ≈318 mOsm with mannitol. 2-APB solution (100 mM) and RN-1734 (14.7 mM) solutions were obtained as previously reported and stocked at −20°C [13, 57].

4.14 | Western Blot and Densitometric Analyses

Western blot was carried out following previously defined procedures [33, 34]. In short, samples containing 25 µg of total protein were separated on SDS–polyacrylamide gels and electro-transferred onto nitrocellulose membranes (Bio-Rad Laboratories). After blocking with 5% BSA in PBS containing 0.05% Tween 20 (PBST), the membranes were incubated with primary antibodies against AQP4 (Santa Cruz Biotechnology) or GFAP (Sigma Aldrich) overnight at 4°C. After washing, they were incubated with horseradish peroxidase-conjugated IgG secondary antibody (Sigma Aldrich) and developed using ECL-Plus (Bio-Rad). Reactive proteins were detected with an enhanced chemiluminescent detection system (ECL Plus, Thermo Scientific, Rockford, IL, USA) and imaged on a Chemidoc imaging system (BioRad, Hercules, CA, USA). The density values of target bands were quantified as the ratio of densitometric signal to total protein levels in Coomassie blue–stained membranes. More details on the experimental procedure are reported in previous studies [33, 34]. Image Lab (BioRad, Hercules, CA, USA) was used for densitometry analysis and GraphPad Prism 8 (GraphPad, San Diego, CA, USA) was employed for the statistical analysis.

4.15 | Water Permeability Measurements

Cell volume changes in primary cultured astrocytes were assessed using a calcein-quenching fluorescence assay, as previously reported [33, 34, 49]. Water permeability tests were carried out 1 day after fAuNCs-BSA treatment and 3 days after astrocyte seeding at a density of [5.000] cells per well on black, clear-bottom, 96-well plates (Corning, New York, USA). Cells were loaded with 10 µM membrane permeable calcein-AM (Molecular Probes, Eugene, Oregon, USA) and fluorescence kinetics in response to changes in extracellular osmolarity were monitored using a FlexStation 3 microplate reader (Molecular Devices, San Jose, CA, USA).Fluorescence was excited at 490 nm and detected at 520 nm using dual monochromators.

Following rinsing with isotonic PBS, an automated volume of either hypertonic solution (0.5 M D-mannitol) or hypotonic solution (NaCl-free PBS) was added to induce the osmotic challenge and achieve the desired final extracellular osmolarity. Under hypotonic conditions, calcein fluorescence intensity increased due to water influx and cell swelling, whereas hypertonic stimulation caused water efflux and cell shrinkage, resulting in decreased fluorescence .

Data acquisition was performed using SoftMax Pro software, and subsequent analyses were carried out with GraphPad Prism (GraphPad Software, La Jolla, CA, USA). The time constant (τ, s) of cell volume variation upon swelling or shrinking was obtained by fitting the data with an exponential function. [33, 34, 49].

4.16 | Calcium Imaging

Variations in free intracellular Ca^{2+} concentration $[Ca^{2+}]_i$ were tracked by calcium microfluorimetry employing the single wavelength fluorescent Ca^{2+} indicator X-RHOD1-AM (Life Technologies, Milan, Italy). Coupling with the acetoxymethyl ester (AM) is necessary for the probe to cross the cell lipid membrane; once inside the cell, these groups are removed by esterase activity and the probe binds calcium ions. NT and fAuNCs-BSA astrocytes were plated on PDL-coated glass and loaded with [1 µM] of X-RHOD1-AM. Measurements of $[Ca^{2+}]_i$ were performed using a fluorescent time-lapse microscope Fluo-Spin up (Crisel Instruments, Rome, Italy) with a 40X water immersion objective and specific filters. Experiments were carried out at room temperature (22°C–24°C). Data acquisition was controlled by Metamorph (Molecular Devices). Pharmacological blockers were diluted in standard bath solution and applied at their respective final concentration [57].

4.17 | Immunofluorescence

The primary antibodies employed were: mouse anti-GFAP (Sigma Aldrich, Milan, Italy) and rabbit anti-Kir 4.1 (Alomone, Jerusalem, Israel) at dilution 1:300, rabbit anti-AQP4 (Cat: sc-20 812; Santa Cruz, Biotechnology, Dallas, Texas, USA) at dilution 1:500, rabbit anti-TRPV4 (Cat: ACC-034; Jerusalem BioPark, Israel) at dilution

1:200, rabbit anti-LRRC8A (VRAC) (produced by Twin Helix). The secondary antibodies employed were: donkey anti-mouse CY3 (Jackson Labs), Alexa488-conjugated donkey anti-rabbit, both at dilution 1:1000. Astrocytes samples were fixed in 4% paraformaldehyde, followed by permeabilization with 0.3% Triton X-100 in PBS. Afterward, samples were incubated with primary antibodies for 3 h and with Alexa conjugated secondary antibodies for 1 h. Additional details on the immunofluorescence procedure are reported in previous studies [33].

F-actin filaments costained with AQP4 were labeled using Phalloidin-FITC (Sigma–Aldrich, Milan, Italy) and imaged with a confocal microscope (Leica TSC-SP8, Leica-Microsystems, Wetzlar, Germany) or with Nikon TE 2000 inverted confocal microscope equipped with 20X and 60X oil-objectives and 400 nm diode, 488 nm Ar+ and 543 nm He–Ne lasers as excitation sources. Fluorescent images of stained astrocytes were also obtained using Nikon Eclipse 80i fluorescent microscope and Fluo-Spin up (Crisel Instruments, Rome, Italy) microscope, provided with 20X and 40X objectives.

The quantification of averaged fluorescence variation in TRPV4 and LRRC8A positive cells was measured using Fiji ImageJ as: mean fluorescence of selected cell area - mean fluorescence of background readings.

4.18 | Nitrogen Vacancy-Based Thermometry

Optically detected magnetic resonance experiments were performed using a fluorescence microscope optical setup equipped with laser light excitation (532 nm, 1 mW) and an amplified microwave source (maximum power 45 dBm). The antenna to deliver the microwave excitation was obtained by placing the uncovered end of a coaxial cable close to the sample. Computer software controlled the system to synchronize the microwave generation and the fluorescence collection. The measurement sequence time was ≈200 s. The data analysis was performed using a homemade Matlab code. Fluorescent ND films (100 nm size, ≈3 ppm NV centers, 1 mg/1 mL in deionized water) were prepared by drop casting on a glass coverslip and let dry. fAuNCs-BSA were deposited at different concentrations in water by drop casting and let them dry on these films.

4.19 | Statistical Analysis

For calcium imaging experiments, cellular fluorescence time series were acquired using Metamorph (Molecular Devices, Sunnyvale, CA, USA), and extracted using Fiji ImageJ software and dynamic-data-exchange Excel file (Microsoft Office 365). Fluorescence intensity variation at each time point was normalized to the initial fluorescence ($\Delta F_t/F_{t0}$) [13, 57].

Representative traces and statistical analyses of calcium imaging and patch-clamp recordings were performed using Microcal Origin 8.5. Bar dot plots were created with Prism Graphpad 8.0.2. Data were compared by one-way ANOVA with Bonferroni post-test, with $p \leq 0.05$ considered statistically significant. The results are expressed as the mean ± Standard Error (SE) of the mean. Sample size (n) for each result is indicated in the corresponding Figure legend. Data were obtained from at least 4 independent experiments.

Data from biological experiments (cell viability, cell differentiation, cell metabolism, and ROS assay) are expressed as the mean ± SE. Sample size (n) for each result is indicated in the corresponding Figure legend. Data were analyzed using one-way ANOVA, with Bonferroni or Dunnett post-tests, with $p \leq 0.05$ considered statistically significant. Bar dot plots were created with Prism Graphpad 8.0.2.

Author Contributions

Roberta Fabbri: conceptualization (supporting); data curation (lead); formal analysis (equal); investigation (lead); methodology (lead); writing – original draft (equal); writing – review & editing (equal). **Karima Jeneh Perry**: conceptualization (equal); data curation (equal); formal analysis (equal); investigation (equal); writing – original draft (equal); writing – review &editing (supporting). **Emanuela Saracino**: formal analysis (equal); investigation (equal); writing – original draft (equal); writing – review & editing (supporting). **Chiara Lazzarini**: data curation (equal); investigation (supporting); methodology (equal); writing – original draft (supporting); writing – review & editing (supporting). **Anna Mariano**: data curation (supporting); formal analysis (supporting); investigation (supporting); methodology (supporting); writing – review & editing (supporting). **Diletta Spennato**: investigation (supporting); methodology (supporting); writing – original draft (supporting); writing – review & editing (supporting). **Maria Grazia Mola**: investigation (supporting); methodology (supporting); writing – original draft (supporting); writing – review & editing (supporting). **Maria Grazia Raucci**: investigation (lead); methodology (supporting); writing – review & editing (supporting). **Alessandro Kovtun**: data curation (supporting); investigation (supporting); methodology (supporting); writing – original draft (supporting); writing – review & editing (supporting). **Marianna Barbalinardo**: investigation (supporting); methodology (supporting). **Giorgia Conte**: formal analysis (supporting); investigation (supporting); methodology (supporting); writing – review & editing (supporting). **Denis Gentili**: investigation (supporting); methodology (supporting). **Marco Caprini**: funding acquisition (supporting); investigation (supporting); methodology (supporting); resources (supporting); writing – review & editing (supporting). **Vincenzo Palermo**: funding acquisition (supporting); project administration (supporting); resources (supporting); writing – review & editing (supporting). **Roberto Zamboni**: funding acquisition (supporting); project administration (supporting); resources (supporting); writing – review & editing (supporting). **Luigi Ambrosio**: funding acquisition (supporting); methodology (supporting); resources (supporting). **Wolfgang Losert**: funding acquisition (supporting); investigation (supporting); methodology (supporting). **Andrea Candini**: data curation (equal); methodology (equal); supervision (equal); writing – original draft (equal); writing – review & editing (equal). **Grazia Paola Nicchia**: conceptualization (supporting); methodology (supporting); resources (supporting); writing – original draft (supporting); writing – review & editing (supporting). **Raj K. Gupta**: funding acquisition (supporting); methodology (equal); writing – original draft (equal); writing – review & editing (supporting). **Valentina Benfenati**: conceptualization (lead); funding acquisition (lead); project administration (lead); resources (lead); supervision (lead); writing – original draft (lead); writing – review & editing (lead). **Shashi P. Karna**: conceptualization (equal); data curation (equal); funding acquisition (equal); writing – original draft (lead); writing – review & editing (lead).

Acknowledgments

The authors are grateful to Dr. Franco Corticelli from IMM-CNR, Bologna, Italy, for his assistance in SEM microscopy and microanalyses. The authors thank Marco Ballestri (ISOF) for help with material characterization and A. Ghirri and M. Affronte (CNR NANO) for their support with the experimental microwave setup. V. B. acknowledge Army Research Office ASTRO-CLUSTER W911NF2520009 (82737-HC-INT), Air Force Office of Scientific Research (AFOSR) - Biophysics Programm

ASTROLIGHT (FA9550-20-1-0386) and ASTROTALK (FA9550-23-1-0736). V. B., G. P. N., G. A., and M. G. R. acknowledge the Air Force Office of Scientific Research (AFOSR) AstroSense (FA9550-25-1-0001).

V. B. and T. P. are supported by NEXTGENERATIONEU (NGEU) funded by the Ministry of University and Research (MUR), National Recovery and Resilience Plan (NRRP), PRIN-PNRR 2022 - NANODYN - P2022Z27NS. G. C. is supported by PNRR MUR project ECS_00000033_ECOSISTER. C. L. is supported by Air Force Office of Scientific Research (AFOSR) ASTROTALK (FA9550-23-1-0736).

W. L. and K. J. P. is are supported by AFOSR IN Biophysics Programm InteNNse (FA9550-25-1-0002). G. C. is supported by Ministero della'Università e della Ricerca (ECS_00000033_ECOSISTER).

Open access publishing facilitated by Consiglio Nazionale delle Ricerche, as part of the Wiley - CRUI-CARE agreement.

Funding

This work has been financially supported by US ARMY, ARL in the projects ASTRO-GOLD- W911NF-21-2-0074, and ASTRO-CLUSTER, W911NF2520009 and by US Air Force of Scientific Research-AFOSR projects ASTROLIGHT-FA9550-20-1-0386 and ASTROTALK - FA9550-23-1-0736 and FA9550-25-1-0001, FA9550-25-1-0002. V. B. and G. P. N. acknowledge Prin-PNRR 2022 Nanodyn. G. C. and E. S. acknowledge the financial support from PNRR MUR project ECS_00000033_ECOSISTER and the Italian Ministry of University and Research (PRIN 20173L7W8K). A. C. thanks CLAN (UniBO and CNR) for the use of the optical microscope and M. Affronte (UniMORE) and A. Ghirri (CNR-NANO) for technical assistance on the microwave setup.

Conflicts of Interest

The authors declare no conflicts of interest.

Data Availability Statement

The data that support the findings of this study are available from the corresponding author upon reasonable request.

References

1. A. Verkhratsky and M. Nedergaard, "Physiology of Astroglia," *Physiological Reviews* 1, no. 98 (2018): 239–389.

2. V. Benfenati and S. Ferroni, "Water Transport Between CNS Compartments: Functional and Molecular Interactions Between Aquaporins and Ion Channels," *Neuroscience* 168 (2017): 926–940.

3. M. M. Halassa, T. Fellin, and P. G. Haydon, "The Tripartite Synapse: Roles for Gliotransmission in Health and Disease," *Trends in Molecular Medicine* 13 (2007): 54–63.

4. E. Scemes and C. Giaume,"Astrocyte Calcium Waves: What They Are and What They Do,"*Glia* 54 (2006):716–725.

5. X. Gu, W. Chen, N. D. Volkow, A. P. Koretsky, C. Du, and Y. Pan, "Synchronized Astrocytic Ca2+ Responses in Neurovascular Coupling during Somatosensory Stimulation and for the Resting State," *Cell Reports* 23 (2018): 3878–3890.

6. M. Santello, N. Toni, and A. Volterra, "Astrocyte Function From Information Processing To Cognition and Cognitive Impairment," *Nature Neuroscience* 22 (2019): 154–166.

7. H. K. Kimelberg and M. Nedergaard, "Functions of Astrocytes and Their Potential As Therapeutic Targets," *Neurotherapeutics: Journal of the American Society for Experimental NeuroTherapeutics* 7 (2010): 338–353.

8. G. Seifert and C. Steinhäuser,"Neuron–Astrocyte Signalling and Epilepsy,"*Experimental Neurology* 244 (2013): 4–10.

9. O. Butenko, D. Dzamba, J. Benesova, et al., "The Increased Activity of TRPV4 Channel in the Astrocytes of the Adult Rat Hippocampus After Cerebral Hypoxia/Ischemia," *PLoS One* 7 (2012): e39959.

10. L. Maiolo, V. Guarino, E. Saracino, et al., "Interfaces: Advanced Materials and Devices to Uncover the Role of Astroglial Cells in Brain Function and Dysfunction," *Advanced Healthcare Materials* 10 (2021): e2001268.

11. J. W. Salatino, K. A. Ludwig, T. D. Y. Kozai, and E. K. Purcell, Glial Responses to Implanted Electrodes in the Brain," *Nature Biomedical Engineering* 2 (2018): 52.

12. R. Fabbri, E. Saracino, E. Treossi, R. Zamboni, V. Palermo, and V. Benfenati,"Graphene glial-interfaces: challenges and perspectives,"*Nanoscale* 13 (2021): 4390–4407.

13. R. Fabbri, A. Scidà, E. Saracino, et al., "Graphene Oxide Electrodes Enable Electrical Stimulation of Distinct Calcium Signalling in Brain Astrocytes," *Nature Nanotechnology* 19 (2024): 1344–1353.

14. S. Yin, J. Liu, Y. Kang, Y. Lin, D. Li, and L. Shao, "Interactions of Nanomaterials with Ion Channels and Related Mechanisms," *British Journal of Pharmacology* 176 (2019): 3754–3774.

15. R. Augustine, A. Hasan, R. Primavera, R. J. Wilson, A. S. Thakor, and B. D. Kevadiya, "Cellular Uptake and Retention of Nanoparticles: Insights on Particle Properties and Interaction with Cellular Components," *Mater.Today Commun* 25 (2020): 101692.

16. J. Xie, Y. Zheng, and J. Y. Ying, "Protein-Directed Synthesis of Highly Fluorescent Gold Nanoclusters," *Journal of the American Chemical Society* 28 (2009): 888–889.

17. T. Q. Yang, B. Peng, B. Q. Shan, et al.,"Origin of the Photoluminescence of Metal Nanoclusters: From Metal-Centered Emission to Ligand-Centered Emission,"*Nanomaterials (Basel)* 10 (2020):261.

18. P. Roberts, J. K. Perry, R. K. Gupta, S. P. Karna, and J. Frechette, "Confinement-Enhanced Luminescence in Protein-Gold Nanoclusters," *Journal of Physical Chemistry Letters* 11 (2020): 10278–10282.

19. N. Kaur, R. N. Aditya, A. Singh, and T. R. Kuo, "Biomedical Applications for Gold Nanoclusters: Recent Developments and Future Perspectives," *Nanoscale Research Letters* 13 (2018): 302.

20. C. Zhang, X. Gao, W. Chen, et al.,"Advances of Gold Nanoclusters for Bioimaging,"*iScience* 25 (2022):105022.

21. L. Chen, A. Black, W. J. Parak, C. Klinke, and I. Chakraborty, Metal Nanocluster-Based Devices: Challenges and Opportunities,"*Aggregate* 3 (2021):1–18.

22. S. M. van de Looij, E. R. Hebels, M. Viola, M. Hembury, S. Oliveira, and T. Vermonden, "Gold Nanoclusters: Imaging, Therapy, and Theranostic Roles in Biomedical Applications," *Bioconjugate Chemistry* 33 (2022): 4–23.

23. A. Cifuentes-Rius, V. G. Deepagan, J. Xie, and Voelcker N. H. Bright, "Future of Gold Nanoclusters in Theranostics," *Acs Applied Materials & Interfaces* 13 (2021): 49581–49588.

24. N. El-Sayed and M. Schneider, "Advances in Biomedical and Pharmaceutical Applications Of Protein-Stabilized Gold Nanoclusters," *Journal of Materials Chemistry B* 8 (2020): 8952–8971.

25. S. Govindaraju, S. R. Ankireddy, B. Viswanath, J. Kim, and K. Yun, "Fluorescent Gold Nanoclusters for Selective Detection of Dopamine in Cerebrospinal Fluid," *Scientific Reports* 7 (2017): 40298.

26. G. Sri Kanaka Durga Vijayalakshmi and N. Puvvada, "Recent Advances in Chemically Engineered Nanostructures Impact on Ischemic Stroke Treatment," *ACS Omega* 8 (2023): 45188–45207.

27. A. L. West, N. M. Schaeublin, M. H. Griep, et al., "In Situ Synthesis of Fluorescent Gold Nanoclusters by Nontumorigenic Microglial Cells," *Acs Applied Materials & Interfaces* 8 (2016): 21221–21227.

28. R. T. Agans, C. E. Dymond, R. E. Jimenez, et al., "Nontumorigenic Microglia Synthesize Strongly Fluorescent Au/Fe Nanoclusters," *Retaining Bioavailability. ACS Omega* 5 (2020): 20983–20990.

29. Q. Yuan, Y. Yao, X. Zhang, J. Yuan, B. Sun, and X. Gao, "The Gold Nanocluster Protects Neurons Directly or via Inhibiting Cytotoxic Secretions of Microglia Cell," *Journal of Nanoscience and Nanotechnology* 19 (2019): 1986–1995.

30. L. Xiao, F. Wei, Y. Zhou, et al., "Dihydrolipoic Acid-Gold Nanoclusters Regulate Microglial Polarization and Have the Potential to Alter Neurogenesis," *Nano Letters* 20 (2020): 478–495.

31. E. R. Gran, F. Bertorelle, H. Fakhouri, et al., "Size and Ligand Effects of Gold Nanoclusters in Alteration of Organellar State and Translocation of Transcription Factors in Human Primary Astrocytes," *Nanoscale* 13 (2021): 3173–3183.

32. J. Ji, A. Moquin, F. Bertorelle, et al., "Organotypic and Primary Neural Cultures As Models to Assess Effects of Different Gold Nanostructures on Glia and Neurons," *Nanotoxicology* 13 (2019): 285–304.

33. T. Posati, A. Pistone, E. Saracino, et al., "A Nanoscale Interface Promoting Molecular and Functional Differentiation of Neural Cells," *Scientific Reports* 6 (2016): 31226.

34. M. G. Mola, E. Saracino, F. Formaggio, et al., "Cell Volume Regulation Mechanisms in Differentiated Astrocytes," *Cellular Physiology & Biochemistry* 55 (2021): 196–212.

35. S. Ferroni, C. Marchini, P. Schubert, and C. Rapisarda, "Two Distinct Inwardly Rectifying Conductances Are Expressed in Long-Term Dibutyryl-Cyclic-AMP Treated Rat Cultured Cortical Astrocytes," *FEBS Letters* 367 (1995): 319–325.

36. M. Chiacchiaretta, M. Bramini, A. Rocchi, et al., "Graphene Oxide Upregulates the Homeostatic Functions of Primary Astrocytes and Modulates Astrocyte-to-Neuron Communication," *Nano Letters* 18 (2018): 5827–5838.

37. V. Benfenati, M. Caprini, M. Nobile, C. Rapisarda, and S. Ferroni, "Guanosine Promotes the Up-Regulation of Inward Rectifier Potassium Current Mediated by Kir4.1 in Cultured Rat Cortical Astrocytes," *Journal of Neurochemistry* 98 (2006): 430–445.

38. V. Benfenati, S. Toffanin, R. Capelli, et al., "A Silk Platform That Enables Electrophysiology and Targeted Drug Delivery in Brain Astroglial Cells," *Biomaterials* 31 (2010): 7883–7891.

39. A. Sagnella, A. Pistone, S. Bonetti, et al., "Effect of Different Fabrication Methods on the Chemo-Physical Properties of Silk Fibroin Films and on Their Interaction with Neural Cells," *Rsc Advances* 6 (2016): 9304–9314.

40. Y. B. Rus, M. Bosmi, S. Maisonneuve, et al., "Versatile One-Pot Synthesis of Gold Nanoclusters and Nanoparticles Using 3,6-(Dipyridin-2-Yl)-(1,2,4,5)-Tetrazine," *RSC Advances* 11 (2021): 7043–7050.

41. L. Dong, M. Li, S. Zhang, et al., "Cytotoxicity of BSA-Stabilized Gold Nanoclusters: In Vitro and In Vivo Study," *Small* 11, no. 21 (2015): 2571–2581.

42. J. V. Sá, S. Kleiderman, C. Brito, et al., "Quantification of Metabolic Rearrangements During Neural Stem Cells Differentiation into Astrocytes by Metabolic Flux Analysis," *Neurochemical Research* 42 (2017): 244–253.

43. M. Agathocleous and W. A. Harris, "Metabolism in Physiological Cell Proliferation and Differentiation," *Trends in Cell Biology* 23 (2013): 484–492.

44. K. M. O'Neill, E. Saracino, B. Barile, et al., "Decoding Natural Astrocyte Rhythms: Dynamic Actin Waves Result from Environmental Sensing by Primary Rodent Astrocytes," *Advanced Biology* 7 (2023): e2200269.

45. V. Jain, S. Bhagat, and S. Singh,"Bovine Serum Albumin Decorated Gold Nanoclusters: A Fluorescence-Based Nanoprobe for Detection of Intracellular Hydrogen Peroxide," *Sensors and Actuators, B: Chemical* 327 (2021):128886–128899.

46. H. Fakhouri, M. P. Bakulić, I. Zhang, et al., "Ligand Impact on Reactive Oxygen Species Generation of Au_{10} and Au_{25} Nanoclusters Upon One- and Two-Photon Excitation," *Communications Chemistry* 6 (2023): 97.

47. E. Saracino, L. Maiolo, D. Polese, et al., "A Glial-Silicon Nanowire Electrode Junction Enabling Differentiation and Noninvasive Recording of Slow Oscillations from Primary Astrocytes," *Advanced Biosystems* 4 (2020): e1900264.

48. V. Benfenati, G. P. Nicchia, M. Svelto, C. Rapisarda, A. Frigeri, and S. Ferroni, "Functional Down-Regulation of Volume-Regulated Anion Channels in AQP4 Knockdown Cultured Rat Cortical Astrocytes," *Journal of Neurochemistry* 100 (2007): 87–104.

49. F. Formaggio, E. Saracino, M. G. Mola, et al., "LRRC8A Is Essential for Swelling-Activated Chloride Current and for Regulatory Volume Decrease in Astrocytes," *FASEB Journal* 33 (2019): 101–113.

50. A. Kumar, L. Xie, C. M. Ta, et al., "SWELL1 Regulates Skeletal Muscle Cell Size, Intracellular Signaling," *Adiposity and Glucose Metabolism. eLife* 9 (2020): e58941.

51. L. Chen, B. König, T. Liu, S. Pervaiz, Y. S. Razzaque, and T. Stauber, "More than Just a Pressure Relief Valve: Physiological Roles of Volume-Regulated LRRC8 Anion Channels," *Biological Chemistry* 400 (2019): 1481–1496.

52. X. Elorza-Vidal, H. Gaitán-Peñas, and R. Estévez, "Chloride Channels in Astrocytes: Structure, Roles in Brain Homeostasis and Implications in Disease," *International Journal of Molecular Sciences* 20 (2019): 1034.

53. K. M. Dunn, D. C. Hill-Eubanks, W. B. Liedtke, and M. T. Nelson, "TRPV4 Channels Stimulate Ca2 -Induced Ca2 Release in Astrocytic Endfeet and Amplify Neurovascular Coupling Responses," *PNAS* 110 (2013): 6157–6162.

54. V. Benfenati, M. Caprini, M. Dovizio, et al., "An Aquaporin-4/Transient Receptor Potential Vanilloid 4 (AQP4/TRPV4) Complex Is Essential for Cell-Volume Control in Astrocytes," *Proceedings of the National Academy of Sciences of the United States of America* 108 (2011): 2563–2568.

55. V. Benfenati, M. Amiry-Moghaddam, M. Caprini, et al., "Expression and Functional Characterization of Transient Receptor Potential Vanilloid-Related Channel 4 (TRPV4) in Rat Cortical Astrocytes," *Neuroscience* 148 (2007): 876–892.

56. V. Benfenati, N. Martino, M. R. Antognazza, et al., "Photostimulation of Whole-Cell Conductance in Primary Rat Neocortical Astrocytes Mediated by Organic Semiconducting Thin Films," *Advanced Healthcare Materials* 3 (2014): 392–399.

57. A. I. Borrachero-Conejo, W. R. Adams, E. Saracino, et al., "Stimulation of Water and Calcium Dynamics in Astrocytes with Pulsed Infrared Light," *FASEB Journal* 34 (2020): 6539–6553.

58. G. S. Terentyuk, G. N. Maslyakova, L. V. Suleymanova, et al., "Laser-Induced Tissue Hyperthermia Mediated by Gold Nanoparticles: Toward Cancer Phototherapy," *Journal of Biomedical Optics* 14 (2009): 021016.

59. M. Honda, Y. Saito, N. I. Smith, K. Fujita, and S. Kawata, "Nanoscale Heating of Laser Irradiated Single Gold Nanoparticles in Liquid," *Optics Express* 19 (2011): 12375–12383.

60. V. M. Acosta, E. Bauch, M. P. Ledbetter, A. Waxman, L. S. Bouchard, and D. Budker, "Temperature Dependence of the Nitrogen-Vacancy Magnetic Resonance in Diamond," *Physical Review Letters* 104 (2010): 070801.

61. G. Kucsko, P. C. Maurer, N. Y. Yao, et al., Nanometre-Scale Thermometry in a Living Cell," *Nature* 500 (2013): 54–58.

62. P. Neumann, I. Jakobi, F. Dolde, et al., "High-Precision Nanoscale Temperature Sensing Using Single Defects in Diamond," *Nano Letters* 13, no. 6 (2013): 2738–2742.

63. R. Schirhagl, K. Chang, M. Loretz, and C. L. Degen,"Nitrogen-Vacancy Centers in Diamond: Nanoscale Sensors for Physics and Biology," *Annual Review of Physical Chemistry* 65 (2014): 83–105.

64. A. Kumar, A. Tan, J. Wong, et al., "Nanotechnology for Neuroscience: Promising Approaches for Diagnostics, Therapeutics and Brain Activity Mapping," *Advanced Functional Materials* 27 (2017): 1700489.

65. A. Panariti, G. Miserocchi, and I. Rivolta, "The Effect of Nanoparticle Uptake on Cellular Behavior: Disrupting or Enabling Functions?," *Nanotechnology, Science and Applications* 5 (2012): 87–100.

66. P. Gao, X. Chang, D. Zhang, et al., "Synergistic Integration of Metal Nanoclusters and Biomolecules as Hybrid Systems for Therapeutic Applications," *Acta Pharmaceutica Sinica B* 11 (2021): 1175–1199.

67. H. Gao, C. Chu, Y. Cheng, et al., "Situ Formation of Nanotheranostics to Overcome the Blood–Brain Barrier and Enhance Treatment of Orthotopic Glioma," *ACS Applied Materials & Interfaces* 12 (2020): 26880–26892.

68. S. Dante, A. Petrelli, E. M. Petrini, et al., "Selective Targeting of Neurons with Inorganic Nanoparticles: Revealing the Crucial Role of Nanoparticle Surface Charge," *ACS Nano* 11 (2017): 6630–6640.

69. D. Maysinger, M. Behrendt, M. Lalancette-Hébert, and J. Kriz, "Real-Time Imaging of Astrocyte Response to Quantum Dots: In Vivo Screening Model System for Biocompatibility of Nanoparticles," *Nano Letters* 7 (2007): 2513–2520.

70. J. McNeill, C. Rudyk, M. E. Hildebrand, and N. Ion Salmaso, "Channels and Electrophysiological Properties of Astrocytes: Implications for Emergent Stimulation Technologies," *Frontiers in Cellular Neuroscience* 15 (2021): 644126.

71. W. Walz and H. K. Kimelberg, "Differences in Cation Transport Properties of Primary Astrocyte Cultures from Mouse and Rat Brain," *Brain Research* 340 (1985): 333–340.

72. H. Kim and X. Xue, "Detection of Total Reactive Oxygen Species in Adherent Cells by 2',7'-Dichlorodihydrofluorescein Diacetate StainingAdherent Cells by 2′,7′-Dichlorodihydrofluorescein Diacetate Staining," *Journal of Visualized Experiments* 160 (2020): 10–3791.

73. E. Eruslanov and S. Kusmartsev, "Identification of ROS Using Oxidized DCFDA and Flow-Cytometry," *Methods in Molecular Biology* 594 (2010): 57–72.

74. G. A. Simms, J. D. Padmos, and P. Zhang, "Structural and Electronic Properties of Protein/Thiolate-Protected Gold Nanocluster with "Staple" Motif: A XAS, L-DOS, and XPS Study," *Journal of Chemical Physics* 131 (2009): 214703-1.

75. M. Barbalinardo, M. Di Giosia, I. Polishchuk, et al., "Retinoic Acid/Calcite Micro-Carriers Inserted in Fibrin Scaffolds Modulate Neuronal Cell Differentiation," *Journal of Materials Chemistry B* 7 (2019): 5808–5813.

Supporting Information

Additional supporting information can be found online in the supporting information section. **Supporting Fig. S1:** Morphological properties of fAuNCs-BSA. A) Scanning Electron Microscopy (SEM) image of dried fAuNCs-BSA casted over a glass coverslip from cell media. Scale bar is 1 μm. Inset: higher magnification image, scale bar is 200 nm. B) Transmission Electron Microscopy image (TEM) investigation of the smallest particles of fAuNCs-BSA. Scale bar is 10 nm. Inset: higher magnification, scale bar is 2 nm. **Supporting Fig. S2:** Impact of fAuNCs-BSA on astrocyte viability and morphology. A, B, C) Low magnification (20X) confocal images of FDA/Hoechst stained astrocytes: NT (A), fAuNCs-BSA [0.1 mM] (B) and fAuNCs-BSA [1 mM] (C) treated cells captured at 3 DIV. Scale bar is 50 μm. D) Bar-dot plot reporting the ratio between the averaged fluorescence of viable cells and of the total number of cells per image (FDA+-Hoechst+/Total number of Hoechst+ cells) calculated on NT and fAuNCs-BSA [0.1 mM] and fAuNCs-BSA [1 mM] treated samples after 3 DIV. n=10 for NT, n=5 for fAuNCs-BSA [0.1 mM] and n=8 for fAuNCs-BSA [1 mM] (n= number of images analyzed). Data are reported as mean ± SE. Statistical significance was calculated via one-way ANOVA with Bonferroni post-test. *: p< 0.05, **: p< 0.01, ***: p< 0.001. No statistical difference was observed between NT and fAuNCs-BSA [0.1 mM] (p=0.75), between NT and fAuNCs-BSA [1 mM] (p=0.08) and between fAuNCs-BSA [0.1 mM] and fAuNCs-BSA [1 mM] (p=0.24). **Supporting Fig. S3:** Effect of fAuNCs-BSA on astrocyte metabolic activity. Bar-dot graph of percentage of reduced Alamar Blue, cell metabolism assay performed on NT, fAuNCs-BSA [1 mM] and HAuCl4 [1mM] treated astrocytes at 3DIV, 14DIV and 21 DIV. For 3 DIV, n=3 for NT, n=3 for fAuNCs-BSA [1mM] and n= 3 for HAuCl4 [1mM]; for 14 DIV, n=5 for NT, n=5 for fAuNCs-BSA [1 mM] and n=12 for HAuCl4 [1mM]; for 21 DIV, n=13 for NT, n=12 for fAuNCs-BSA [1 mM] and n=9 for HAuCl4 [1mM] (n=number of measurements). Data are reported as mean ± SE. Statistical significance was calculated via one-way ANOVA with Bonferroni post-test. *: p< 0.05, **: p< 0.01, ***: p< 0.001. Statistical difference was observed in the % of reduced AB between NT and fAuNCs-BSA [1 mM] at 21 DIV (p=0.0039). No statistical difference was observed in the % of reduced AB between NT and fAuNCs-BSA [1 mM] at 3 DIV (0.24) and at 14 DIV (0.84). Statistical difference was observed in the % of reduced AB between NT and HAuCl4 [1mM] at 3 DIV (p=0.05), at 14 DIV (p=5.83 10-4), at 21 DIV (p=1.93 10-4). Statistical difference was observed in the % of reduced AB between fAuNCs-BSA [1 mM] and HAuCl4 [1mM] at 14 DIV (p=14.26 10-4). No statistical difference was observed in the % of reduced AB between fAuNCs-BSA [1 mM] and HAuCl4 [1mM] at 3 DIV (p=0.85) and at 21 DIV (p=0.06). **Supporting Fig. S4:** fAuNCs-BSA is not inducing Reactive Oxygen Species (ROS). Averaged DCFH-DA fluorescence intensity, which correlates with the intracellular concentration of ROS.1,2 Data are reported as mean ± SE (n = 3, n=number of experiments for each condition). Statistical significance was calculated via one-way ANOVA test with post hoc Dunnett's test. ****p < 0.0001. **Supporting Fig. S5:** Effect of fAuNCs-BSA on electrophysiological properties of astrocytes. Typical current traces recorded stimulating astrocytes with a voltage ramp protocol (inset to panel A) from -120 to +60 mV (500 ms) with Vh=-60 mV, in NT (A) and fAuNCs-BSA [1 mM] treated (B) astrocytes in standard condition (black line, CTRL) in presence of potassium in the intracellular and extracellular solution, at 14 DIV from the treatment with fAuNCs-BSA [1mM]. **Supporting Fig. S6:** Effect of fAuNCs-BSA on TRPV4 and LRRC8-A in astrocytes. Confocal microscopy images of primary cortical astrocytes stained with TRPV4 (A, B) and with LRRC8-A (C, D) antibodies in NT (A, C) and fAuNCs-BSA [1mM] treated (B, D) conditions. Scale bar is 50 μm. E) Bar-dot graph representing the quantification of averaged fluorescence variation measured in TRPV4 and LRRC8-A stained- astrocytes, in NT and fAuNCs-BSA [1mM] treated conditions. For TRPV4, n=58 for NT and n=47 for fAuNCs-BSA [1mM]; for LRRC8-A, n=6 for NT and n=38 for fAuNCs-BSA [1mM] (n=number of images analyzed). Data are reported as mean ± SE. Statistical significance was calculated via one-way ANOVA with Bonferroni post-test. *: p< 0.05, **: p< 0.01, ***: p< 0.001. No statistical difference was observed between NT and fAuNCs-BSA [1mM] for TRPV4 (p=0.35) and for LRRC8-A (p=0.4) -stained astrocytes. **Supporting Fig. S7:** Effect of fAuNCs-BSA on AQP4 expression in astrocytes. Confocal images of primary cortical astrocytes stained with FITC Phalloidin (green staining)/ AQP4 (red staining) in NT (A, B) and fAuNCs-BSA [1mM] treated cells (C, D). The images show the response of astrocytes' morphology and cytoskeleton and the expression of the water channel AQP4 in NT (A, B) and fAuNCs-BSA [1mM] (C, D) treated cells. Scale bar is 40 μm. E, F) Representative western blot analysis of AQP4 expression in primary astroglial cultures in NT and fAuNCs-BSA [1mM] treated cells after 24hrs. The immunoblotting (E) and quantification of the expression level of AQP4 (F) notes that the expression level of AQP4 decrease, not significantly, between NT and fAuNCs-BSA treated astrocytes (n=4, n=number of experiments for each condition). Data are reported as mean ± SE. Statistical significance was calculated via one-way ANOVA with Bonferroni post-test. *: p< 0.05, **: p< 0.01, ***: p< 0.001. **Supporting Fig. S8:** Statistical analysis of calcium imaging experiments performed on NT cells and fAuNCs-BSA [1mM] treated cells, in standard extracellular solution (CTRL, black bar for NT and red bar for fAuNCs-BSA [1mM]), and under pharmacological treatment by removing calcium

from the extracellular solution (0 EXT Ca^{2+}, blue bars) and upon the exposition to 2-Aminoethoxydiphenyl borate [100 μM] (2APB, inhibitor of IP3, orange bars) and to RN-1734 [10 μM] (RN, inhibitor of TRPV4, green bars). A-C) Bar-dot graphs representative of the experiments conducted on astrocytes, showing A) averaged number of peaks, B) averaged onset time (s), C) averaged time to peak (s). For CTRL condition, n=75, N=9 for NT and n=230, N=9 for fAuNCs-BSA [1mM]. For 0 EXT Ca^{2+} condition, n=26, N=3 for NT and n=39, N=3 for fAuNCs-BSA [1mM]. For 2APB condition, n=17, N=3 for NT and n=14, N=3 for fAuNCs-BSA [1mM]. For RN condition, n=48, N=3 for NT and n=43, N=3 for fAuNCs-BSA [1mM] (n=number of cells, N=number of independent experimental trials). Data are reported as mean ± SE. Statistical significance was calculated via one-way ANOVA with Bonferroni post-test. *: $p< 0.05$, **: $p< 0.01$, ***: $p< 0.001$-. **Supporting Fig. S9:** Scheme of effects of [1mM] fAuNCs-BSA in astrocytes at different time points and of possible mechanism beyond. A) 1-Scheme representing the protocol for treatment of astrocytes (NT) with [1mM] fAuNCs-BSA. 2- Blue bar at the bottom represents different time points of morphological molecular and functional analyses performed to analyze effects of [1mM] fAuNCs-BSA with no light exposure over longer term. The scheme highlights that the treatment with fAuNCs-BSA leads to morphological differentiation of astrocytes. 3- The treatment with fAuNCs-BSA does not induce ROS production (horizontal black arrow) or alter potassium current (horizontal violet arrow). Morphological differentiation is accompanied by the up-regulation of whole-cell chloride conductance (up yellow arrow), enhanced RVD capabilities (up green arrow), and increased calcium signaling via IP_3 release from intracellular stores and through extracellular calcium entry via TRPV4 (up red arrows). We hypothesize that $[Ca^{2+}]$i released via IP3 path can bind TRPV4 and sensitize it to cell volume variations to initiate RVD. B) Scheme of experimental protocol (1) and of patch-clamp experiments (2) performed at 3DIV upon acute photostimulation (λex=450 nm) of [1mM] fAuNCs-BSA treated astrocytes. 3- The photostimulation elicits a decrease in whole cell potassium current (down violet arrow), possibly duo to a photothermal effect (up red arrow, DT°C). We cannot rule out that temperature increase may affect calcium signaling through the thermosensitive TRPV4 channel or the IP3 pathway. **Supporting Table. S1:** Statistics of calcium imaging experiments performed in fAuNCs-BSA –treated astrocytes. Number of experimental trials, replicates and cells analyzed for calcium imaging experiments performed on NT and fAuNCs-BSA [1mM] treated cells, for each condition.